Shape-Effect in the Effective Laws of Plain and Rubberized Concrete

E. Ferretti[1]

Abstract: The procedure of the effective law outlined in this paper [Ferretti (2001); Ferretti and Di Leo (2003); Ferretti (2004b)] is an experimental procedure for identifying the constitutive law in uniaxial compression of brittle heterogeneous materials, and is based on the physical, analytical and numerical discussions about the existence or otherwise of strain-softening [Ferretti (2004a); Ferretti (2005)]. This procedure allows us to correct several incongruities that characterize the average stress versus average strain diagrams: it produces evidence against strain-softening in uniaxial compression [Ferretti (2004b)], whose existence may be questioned from a physical point of view [Ferretti (2004a); Ferretti (2005)], it provides effective stress versus effective strain laws that are size-effect insensitive [Ferretti (2004b)] and identifies Poisson's ratio and volumetric strain, which are independent of the degree of damage during the compression test [Ferretti (2004c)], as should be the case for all constitutive parameters. The procedure also allows us to explain the gradual change of shape in the average stress versus average strain laws when a confinement pressure is applied to the specimen [Ferretti and Di Leo (2003)]. Moreover, the procedure emphasizes how the final stage in compressed concrete specimens is largely characterized by the propagation of a macro-crack, rather than by crushing. This puts a question mark on the existence of creep, which, according to the identified effective parameters, seems mainly to be a structural effect due to crack propagation [Ferretti and Di Leo (2008)]. In this paper, the identification procedure of the effective law is applied to cubic and cylindrical concrete specimens, in order to verify whether or not the effective law is sensitive to shape-effect. Two different concrete mixtures were used, the one of plain and the other of rubberized concrete. New relationships were also proposed for design purposes, both for plain and rubberized concrete.

Keywords: Strain-softening, Constitutive Parameters Identification, Damage, Creep, FRP wrapping, Nonlocality, Cell Method.

---

[1] DICAM, Facoltà di Ingegneria, Alma Mater Studiorum, Università di Bologna, Viale Risorgimento 2, 40136 (BO), Italy.

1 Introduction

The main motivation at the basis of the identification procedure of the effective law for brittle materials, such as concrete, is the idea that the structural behavior of the specimen used in uniaxial compression tests must be differentiated from the constitutive behavior of the specimen material. This idea emanates from the failure mechanism of brittle specimens, which is characterized by the propagation of macro-cracks (Fig. 1) that modify the resistant structure of the specimen (Fig. 2) throughout the compression test. As a consequence, an identifying model, and not a scale factor (Fig. 3), is needed in order to derive the stress-strain law, $\sigma - \varepsilon$, which pertains to the material, from the experimental load-displacement law, $N - u$, which pertains to the structure. This means that the $\sigma - \varepsilon$ and $N - u$ curves may not be homothetic, posing the question about the possible plot of the material law, which, in the following, will be called the effective law, $\sigma_{eff} - \varepsilon_{eff}$, in order to distinguish it from the average stress versus average strain law, $\bar{\sigma} - \bar{\varepsilon}$, traditionally assumed as the constitutive law.
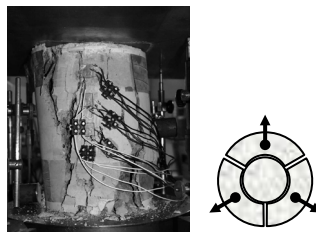
Figure 1: Vertical cracks on the surface of a concrete specimen originated by the splitting of incoherent material isolated by the propagation of internal macro-cracks

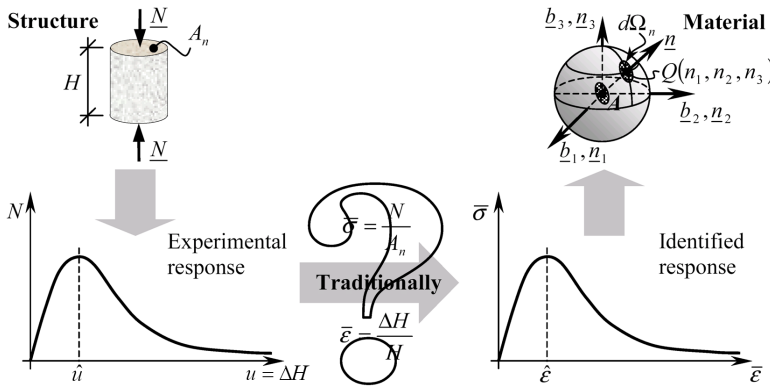Figure 2: Concrete specimen at the end of the test, after removal of the outer part

Figure 3: Traditional identification of mono-axial constitutive law by experimental tests

Ferretti and Di Leo (2003) and Ferretti (2005) have widely discussed how some theoretical research of the last century [Hadamard (1903); Hudson, Brown, and Fairhurst (1971); Dresher and Vardoulakis (1982); Bergan (1983); Hegemier and Read (1983); Sandler and Wright (1983); Wu and Freud (1983)], demonstrating that strain-softening is not a material property, and subsequently forgotten when the experimental $N - u$ laws, which are the softening laws, seemed to state the opposite, assume a new significance in this context. Ferretti (2004a) likewise moves in this direction, analyzing the problem of the existence of strain-softening from analytical and physical perspectives.

Ferretti and Di Leo (2003) and Ferretti (2004b) presented some details of the identification procedure of the effective law, providing results for cylinders of varying $H/(2R)$ ratio (slenderness ratio). These results actually show that the effective law is not a softening law, supporting the aforementioned theoretical research with an experimental procedure. Moreover, the effective laws for varying $H/(2R)$ ratios do not seem to be sensitive to size-effect, which must be the case for a properly identified constitutive relationship.

The effective law's insensitiveness to parameters that are not related to the material directly is further investigated by Ferretti (2004c), who provides a discussion on the proper identification of Poisson's ratio and volumetric strain (dilatancy). It was found that Poisson's ratio is almost independent of the longitudinal strain, while it grows indefinitely when it is identified using $\bar{\varepsilon}$ instead of ε_{eff}. Moreover, it was found that concrete never exhibits dilatancy. What we know as concrete dilatancy [Brace, Paulding, and Scholz (1966); Di Leo, Di Tommaso, and Merlari (1979)] is an apparent effect, caused by an identification technique that

inadequately evaluates the influence on the acquired data of a failure mechanism with splitting of the material isolated by the propagation of the dominant crack (Fig. 2). A further consequence of this inadequate identification technique is the common belief that concrete exhibits a viscous behavior when subjected to constant loads. Indeed, the identification procedure of the effective law shows that displacement time-dependence is determined, mostly, not by material viscosity, but by crack propagation [Ferretti and Di Leo (2008)].

In conclusion, the effective law is not affected by some of the incongruities, such as size effect, that burden the $\bar{\sigma} - \bar{\varepsilon}$ law, which should be constitutive, that is, only depending on the material. The constancy of Poisson's ratio also leads us to conclude that the $\sigma_{eff} - \varepsilon_{eff}$ law is more representative of the constitutive behavior than the $\bar{\sigma} - \bar{\varepsilon}$ law, since even Poisson's ratio itself should be dependent on the material only. Nevertheless, one further point must be discussed before the effective law can be adopted as a constitutive law useful in numerical analyses, specifically, is the effective law suitable for modeling nonlocal effects? The question arises from the observation that the effective law is a local material law, with the stress at a given point depending exclusively on the current values, and also on the previous history, of deformation at that point only. Since research carried out over many years has shown that the classical local continuum concept, leading to constitutive models falling within the category of simple nonpolar materials [Noll (1972)], does not seem to be adequate for modeling heterogeneous materials [Duhem (1893); Rayleigh (1918); Oseen (1933); Chandrasekhar (1950); Hodgkin (1964); Krumhansl (1965); Rogula (1965); Eringen (1966); Kunin (1966); Kröner (1968); Edelen, Green, and Laws (1971); Eringen (1972); Eringen, and Edelen (1972); Eringen, and Kim (1974); Eringen, Speziale, and Kim (1977); Eringen (1981); Rogula (1982); Eringen (1983); Bažant, Belytschko, and Chang (1984); Bažant, and Chang (1984); Pijaudier-Cabot, and Bažant (1987); Bažant, and Lin (1988a); Bažant, and Lin (1988b); Bažant, and Pijaudier-Cabot (1988); Saouridis (1988); Bažant, and Pijaudier-Cabot (1989); Bažant, and Ožbolt (1990); Bažant, Tabbara, Kazemi, and Pijaudier-Cabot (1990); Bažant (1991); Saouridis, and Mazars (1992); Schlangen, and van Mier (1992); Planas, Elices, and Guinea (1993); Schlangen (1993); Bažant (1994); Huerta, and Pijaudier-Cabot (1994); Leblond, Perrin, and Devaux (1994); Nilsson (1994); Vermeer, and Brinkgreve (1994); Jirásek, and Bažant (1995); Tvergaard, and Needleman (1995); Drugan, and Willis (1996); Ožbolt, and Bažant (1996); Planas, Guinea, and Elices (1996); Strömberg, and Ristinmaa (1996); Nilsson (1997); van Mier (1997); Jirásek (1998a); Jirásek (1998b); Jirásek, and Zimmermann (1998); Needleman, and Tvergaard (1998); Borino, Fuschi, and Polizzotto (1999); Jirásek (1999); Chen, Wu, and Belytschko (2000); Hu, and Wittmann (2000); Jirásek, and Bažant (2001); Gao, and

Huang (2001); Luciano, and Willis (2001); Bažant, and Jirásek (2002); Jirásek, and Patzák (2002); Jirásek, and Rolshoven (2002)], it follows that the answer may seem negative. This is not the case, since it has been shown [Ferretti (2005)] that nonlocal constitutive laws between stress and strain tensors are not strictly needed to construct a material model. They are required only if a differential formulation is used, since differential operators are local. The effective law is suitable for modeling nonlocal effects if used with a formulation which is nonlocal in itself, such as the Cell Method (CM) [Ferretti (2005)].

In order to use the effective law in modeling, the separation between structural and material behavior must also be taken into account in numerical analyses. That is, we must allow the domain to upload when a crack propagation condition is reached, causing the resistant structure to modify during modeling. In Ferretti (2003), a CM code for modeling crack propagation in concrete cylinders in uniaxial compression was presented for the first time, in which a nodal relaxation technique was used for uploading the domain. The cylinders have different $H/(2R)$ ratios, as did the cylinders used in Ferretti and Di Leo (2003). It was found that, using the same effective law for all cylinders, different $N - u$ curves were obtained for different $H/(2R)$ ratios and all the $N - u$ curves are softening curves. The numerical results fit well with the experimental results of Ferretti and Di Leo (2003). In conclusion, it was numerically verified that the propagation of a macro-crack in compressed cylinders is the single factor responsible for the softening behavior in the $N - u$ curves when the material is not a strain-softening material. The different shape of the $N - u$ curves in function of the $H/(2R)$ ratio is explained once again by the propagation of the macro-crack, since the crack propagation speed depends on the $H/(2R)$ ratio, causing a faster decrement of the resistant area for higher $H/(2R)$ ratios. The dependence of the shape of the $N - u$ curves on crack propagation only has also been numerically verified in Ferretti and Di Leo (2003) and Ferretti (2005), where $N - u$ curves are provided for cylinders wrapped in a differing number of FRP sheets. Even in this case, the same effective law was used for all cylinders, and different $N - u$ curves were obtained for the different numbers of FRP sheets. This can be explained by the fact that crack propagation speed depends upon the number of sheets, with a slower decrement of the resistant area occurring for a higher number of sheets.

The effective law has also been used to model crack propagation in four-point bending concrete beams [Ferretti (2004d)], pullout testing in concrete panels [Ferretti (2004e)], shear testing in masonry walls [Ferretti, Casadio, and Di Leo (2008)], and tensioned concrete plates [Ferretti (2009)], in all cases giving the correct crack propagation path and useful information on stress distribution during propagation. In particular, in Ferretti, Casadio, and Di Leo (2008), the CM code was modified

so that multiple-cracks propagation can be modeled.

In the following sections, the main findings of the research into the effective law are summarized clearly, in order to give a thorough explanation of the experimental program and related data processing, presented here, to readers with no previous experience of this identification technique.

1.1 Discussion on the analytical well-posedness of strain-softening

Let us consider the identification procedure of the effective stress using experimental data acquired for concrete cylindrical specimens in uniaxial compression. The compression tests are performed in displacement control, by increasing the relative displacement between the platens of the testing machine, Δu, monotonically. Of the two platens of the compression testing machine, the upper one is attached to a screw, which passes through the cross-head plate, and can be raised or lowered to adjust for initial clearance, while the lower platen is movable. Since loading takes place through the upward movement of the lower platen, while the upper platen does not move, the relative displacement Δu is equal to the upward displacement of the lower platen, u:

$$\Delta u = u. \tag{1}$$

The acquired data are the impressed displacement given by the lower platen, u, and the subsequent external load, $N = N(u)$, measured by the load measuring device attached to the upper platen. As is well known, plotting the $N - u$ relationship shows, at first, an ascending branch, then a peak and a descending branch, also called softening branch (Fig. 3).

In the assumption that the specimen used for uniaxial compression testing modifies its resistant structure during the test, due to crack propagation, the progressive normalized decrement of area can be estimated at each test step as:

$$D = D(u) = \frac{A_n - A_{res}(u)}{A_n} = 1 - \frac{A_{res}(u)}{A_n}, \tag{2}$$

where A_n is the nominal area (Fig. 3) and A_{res} is the resistant area, which varies with the test step. D varies from 0 (test beginning, when the crack has not yet enucleated and $A_{res} = A_n$) to 1 (specimen crushing) and gives a measure of how much the crack propagation has affected the resistant area.

In accordance with the scalar theory of Fracture Mechanics with Damage, D will be the damage parameter in the following. The analogy with the operation process of Fracture Mechanics with Damage is limited to Eq. (2). Indeed, in Fracture

Mechanics with Damage, D has an analytic formulation and is considered to be uniformly distributed on A_n. Here, D is experimentally evaluated and all the damage is considered to be localized within the volume of incoherent material.

Using the last equality in Eq. (2), the resistant area can be expressed in function of the damage parameter as:

$$A_{res} = A_{res}(u) = A_n (1 - D(u)). \tag{3}$$

The effective stress, σ_{eff}, is defined to be the average stress acting on the resistant area, A_{res}:

$$\sigma_{eff} = \sigma_{eff}(u) = \frac{N(u)}{A_{res}(u)}. \tag{4}$$

Since, to conserve equilibrium along the load direction, we can write:

$$N(u) = \bar{\sigma}(u) A_n, \tag{5}$$

where $\bar{\sigma}$ is the average stress on the nominal area A_n, the effective stress in Eq. (4) can be also expressed as:

$$\sigma_{eff} = \sigma_{eff}(u) = \frac{A_n}{A_{res}(u)} \bar{\sigma}(u). \tag{6}$$

By defining the average strain along the load direction, $\bar{\varepsilon}$, as the specimen axial contraction, ΔH, divided by the gauge length, H (specimen height, see Fig. 3):

$$\bar{\varepsilon} = \frac{\Delta H}{H} = \frac{\Delta u}{H} = \frac{u}{H}, \tag{7}$$

it is possible to express the effective stress in the variable $\bar{\varepsilon}$, as $\sigma_{eff} = \sigma_{eff}(\bar{\varepsilon})$, and plot it in the $\sigma_{eff} - \bar{\varepsilon}$ plane. Obviously, in our assumption of a modifying resistant structure for crack propagation, $\bar{\varepsilon}$ has no physical meaning and, strictly speaking, it could not be called the average strain either. As a matter of fact, Eq. (7) gives a strain for the continuum theory only. Here, $\bar{\varepsilon}$ is a normalized (relative) displacement, which originates, in part, by material strain and, in part, by a crack opening. This position alone represents the main difference between the identification procedure of the effective law and the traditional identification procedure. The estimation of the material strain, called the effective strain, ε_{eff}, will be shown in §1.2 according to the identification procedure of the effective law.

The question that we want answer in this section is whether or not the sign of the first derivative of the function $\sigma_{eff}(\bar{\varepsilon})$ is known in the $\sigma_{eff} - \bar{\varepsilon}$ plane. That is, we

want know whether or not it is possible to find analytically whether the $\sigma_{eff} - \bar{\varepsilon}$ relationship also has a softening branch. In order to answer this question, we have rewritten Eq.(4) using the change of variable - from u to $\bar{\varepsilon}$ - expressed in Eq. (7) by the equality between the first and the last terms:

$$\sigma_{eff} = \sigma_{eff}(\bar{\varepsilon}) = \frac{N(\bar{\varepsilon})}{A_{res}(\bar{\varepsilon})}. \tag{8}$$

We then find the first derivative of Eq. (8), in the variable $\bar{\varepsilon}$:

$$\frac{d\sigma_{eff}(\bar{\varepsilon})}{d\bar{\varepsilon}} = \frac{\frac{dN(\bar{\varepsilon})}{d\bar{\varepsilon}}A_{res}(\bar{\varepsilon}) - N(\bar{\varepsilon})\frac{dA_{res}(\bar{\varepsilon})}{d\bar{\varepsilon}}}{A^2_{res}(\bar{\varepsilon})}. \tag{9}$$

If we define $\hat{\varepsilon} = \hat{u}/H$ to be the value of the average strain, $\bar{\varepsilon}$, giving the maximum load (Fig. 3), then:

$$N(\bar{\varepsilon})|_{\bar{\varepsilon}=\hat{\varepsilon}} = N_{\max}, \tag{10}$$

and we can now observe that:

- N is monotonically non-decreasing until the peak of the relationship $N - \bar{\varepsilon}$:

$$\frac{dN(\bar{\varepsilon})}{d\bar{\varepsilon}} \geq 0 \quad 0 \leq \bar{\varepsilon} \leq \hat{\varepsilon}, \tag{11}$$

and monotonically strictly non-increasing beyond the peak:

$$\frac{dN(\bar{\varepsilon})}{d\bar{\varepsilon}} < 0 \quad \bar{\varepsilon} > \hat{\varepsilon}, \tag{12}$$

- since A_{res} can never increase during the test, while it decreases at each crack propagation, A_{res} is monotonically non-increasing in all its domain of definition:

$$\frac{dA_{res}(\bar{\varepsilon})}{d\bar{\varepsilon}} \leq 0 \quad \forall \bar{\varepsilon}, \tag{13}$$

and can have a zero tangent only in the neighborhood of the origin, where the material is in its linear-elastic state:

$$\left.\frac{dA_{res}(\bar{\varepsilon})}{d\bar{\varepsilon}}\right|_{\bar{\varepsilon}=0} = 0, \tag{14}$$

$$\left.\frac{dA_{res}(\bar{\varepsilon})}{d\bar{\varepsilon}}\right|_{\bar{\varepsilon}=\hat{\varepsilon}} < 0. \tag{15}$$

From Eqs. (11), (13) and (15), it immediately follows that the numerator in Eq. (9) is strictly positive for $0 \leq \bar{\varepsilon} \leq \hat{\varepsilon}$. Consequently, the sign of $d\sigma_{eff}/d\bar{\varepsilon}$ is also strictly positive for $0 \leq \bar{\varepsilon} \leq \hat{\varepsilon}$:

$$\frac{d\sigma_{eff}(\bar{\varepsilon})}{d\bar{\varepsilon}} > 0 \quad 0 \leq \bar{\varepsilon} \leq \hat{\varepsilon}. \tag{16}$$

In particular, for $\bar{\varepsilon} = \hat{\varepsilon}$, Eq. (9) assumes the value:

$$\left.\frac{d\sigma_{eff}(\bar{\varepsilon})}{d\bar{\varepsilon}}\right|_{\bar{\varepsilon}=\hat{\varepsilon}} = -\left.N(\bar{\varepsilon})\right|_{\bar{\varepsilon}=\hat{\varepsilon}} \frac{\left.\frac{dA_{res}(\bar{\varepsilon})}{d\bar{\varepsilon}}\right|_{\bar{\varepsilon}=\hat{\varepsilon}}}{\left.A_{res}^2(\bar{\varepsilon})\right|_{\bar{\varepsilon}=\hat{\varepsilon}}} > 0, \tag{17}$$

where the strict inequality comes from Eq. (15).

Eq. (17) implies the following important result: a point with a strictly positive tangent in the $\sigma_{eff} - \bar{\varepsilon}$ relationship corresponds to the peak in the $N - u$ relationship. Thus, the peak of the $N - u$ relationship does not generate a peak in the $\sigma_{eff} - \bar{\varepsilon}$ relationship. This is a significant result, since it was obtained without having introduced any other assumptions about the plot of the law describing the decrement of A_{res}, except the physically justifiable condition of a non zero tangent in correspondence of the maximum load. The same result obtained for the sign of the tangent can be transposed to the $\sigma_{eff} - \varepsilon_{eff}$ relationship, since substituting $\bar{\varepsilon}$ with ε_{eff} is simply another change of variable.

As far as the sign of Eq. (9) for $\bar{\varepsilon} > \hat{\varepsilon}$ is concerned, this depends on the value of ρ, the ratio between the two terms in the numerator of Eq. (9):

$$\rho = \frac{\frac{dN(\bar{\varepsilon})}{d\bar{\varepsilon}} A_{res}(\bar{\varepsilon})}{N(\bar{\varepsilon}) \frac{dA_{res}(\bar{\varepsilon})}{d\bar{\varepsilon}}}. \tag{18}$$

The result is:

$$0 \leq \rho \leq 1 \Rightarrow \frac{d\sigma_{eff}(\bar{\varepsilon})}{d\bar{\varepsilon}} \geq 0 \quad \bar{\varepsilon} > \hat{\varepsilon}; \tag{19a}$$

$$\rho > 1 \Rightarrow \frac{d\sigma_{eff}(\bar{\varepsilon})}{d\bar{\varepsilon}} < 0 \quad \bar{\varepsilon} > \hat{\varepsilon}. \tag{19b}$$

One can also examine the sign for $\bar{\varepsilon} > \hat{\varepsilon}$ of the first derivative of q, which is defined as the ratio between the normalized resistant area, A_{res}/A_n, and the normalized load, $N/N_{\max}$:

$$q(\bar{\varepsilon}) = \frac{\frac{A_{res}(\bar{\varepsilon})}{A_n}}{\frac{N(\bar{\varepsilon})}{N_{\max}}} = \frac{\bar{\sigma}_{\max}}{\sigma_{eff}(\bar{\varepsilon})}. \tag{20}$$

The derivative gives:

$$\frac{dq(\bar{\varepsilon})}{d\bar{\varepsilon}} = -\bar{\sigma}_{\max} \frac{\frac{d\sigma_{eff}(\bar{\varepsilon})}{d\bar{\varepsilon}}}{\sigma_{eff}^2(\bar{\varepsilon})} = -\bar{\sigma}_{\max} \frac{\frac{dN(\bar{\varepsilon})}{d\bar{\varepsilon}} A_{res}(\bar{\varepsilon}) - N(\bar{\varepsilon}) \frac{dA_{res}(\bar{\varepsilon})}{d\bar{\varepsilon}}}{N^2}. \tag{21}$$

From Eqs. (21) and (18), it can be observed that the sign of $dq/d\bar{\varepsilon}$ is determined by ρ:

$$0 \leq \rho \leq 1 \Rightarrow \frac{dq(\bar{\varepsilon})}{d\bar{\varepsilon}} \leq 0 \quad \bar{\varepsilon} > \hat{\varepsilon}; \tag{22a}$$

$$\rho > 1 \Rightarrow \frac{dq(\bar{\varepsilon})}{d\bar{\varepsilon}} > 0 \quad \bar{\varepsilon} > \hat{\varepsilon}. \tag{22b}$$

On the other hand, the sign of $dq/d\bar{\varepsilon}$ follows directly from Eqs. (19) and the first equality in Eq. (21), which states that $dq/d\bar{\varepsilon}$ and $d\sigma_{eff}/d\bar{\varepsilon}$ have opposite signs for all $\bar{\varepsilon}$.

Combining Eqs. (19) and (22) and keeping in mind the meaning of q, expressed by Eq. (20), we can state that the slope for $\bar{\varepsilon} > \hat{\varepsilon}$ of the $\sigma_{eff} - \bar{\varepsilon}$ plot is positive when the normalized resistant area decreases faster than the normalized load:

$$\frac{dq(\bar{\varepsilon})}{d\bar{\varepsilon}} \leq 0 \Rightarrow \frac{d\sigma_{eff}(\bar{\varepsilon})}{d\bar{\varepsilon}} \geq 0 \quad \bar{\varepsilon} > \hat{\varepsilon}, \tag{23}$$

while it is negative when the normalized resistant area decreases slower than the normalized load:

$$\frac{dq(\bar{\varepsilon})}{d\bar{\varepsilon}} > 0 \Rightarrow \frac{d\sigma_{eff}(\bar{\varepsilon})}{d\bar{\varepsilon}} < 0 \quad \bar{\varepsilon} > \hat{\varepsilon}. \tag{24}$$

Thus, the existence of a strain-softening branch for $\bar{\varepsilon} > \hat{\varepsilon}$ depends on the law describing the resistant area, A_{res}, or, which is the same as for Eq. (2), on the law describing the damage parameter, D.

In conclusion, we have demonstrated that the sign of $d\sigma_{eff}/d\bar{\varepsilon}$ is strictly positive for $0 \leq \bar{\varepsilon} \leq \hat{\varepsilon}$ (Fig. 4), whereas it is only known when the law describing D is known for $\bar{\varepsilon} > \hat{\varepsilon}$.

In order to make it possible to discuss the slope of the $\sigma_{eff} - \bar{\varepsilon}$ relationship also for the $\bar{\varepsilon} > \hat{\varepsilon}$ range, we have adopted a procedure for identifying D experimentally, which will be shown in §1.2.
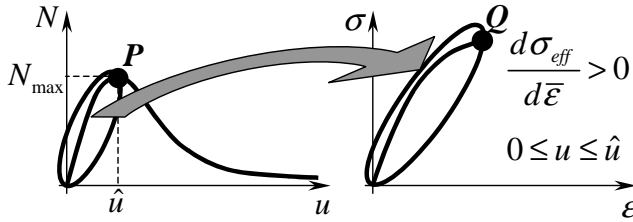
Figure 4: Results of the algebraic analysis on $d\sigma_{eff}/d\bar{\varepsilon}$

1.2 The identification procedure of the effective law

In order to evaluate $D = D(\bar{\varepsilon})$ experimentally, two damage laws can be employed. The first damage law, D_1 [Daponte and Olivito (1989)], relates the damage parameter to the variation of the microseismic signal velocity, V, at the current test step:

$$D_1 = 1 - \frac{V}{V_0}, \tag{25}$$

where V_0 is the initial microseismic signal velocity.

To evaluate the damage parameter in a uniaxial compression test, the path along which the microseismic velocity can be evaluated is one diameter of the middle cross-section (Fig. 5.a).
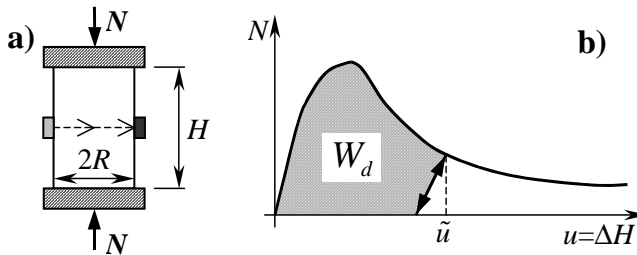
Figure 5: a) Test set-up for the acquisition of D_1; b) Evaluation of W_d for the acquisition of D_2

The second damage law, D_2 [Ferretti and Di Leo (2003); Ferretti (2004b)], relates the damage parameter to the dissipated energy at the current test step, W_d (Fig. 5.b), and the total dissipated energy, $W_{d,t}$:

$$D_2 = \frac{W_d}{W_{d,t}}. \tag{26}$$

The experimental laws describing D_1 and D_2 are very similar. These, together with Eqs. (3) and (4), allow us to identify the effective stress, σ_{eff}, as:

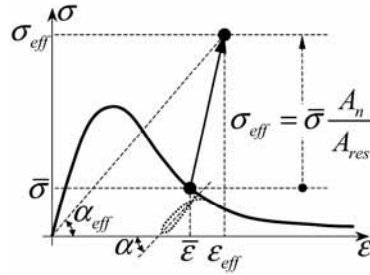$$\sigma_{eff} = \frac{N}{A_n}\frac{1}{1-D} = \bar{\sigma}\frac{1}{1-D}. \tag{27}$$

Figure 6: Identification of ε_{eff} starting from the known values of σ_{eff} (Eqs. (4), (3) and (7)) and α_{eff}

The effective strain ε_{eff} is identified by considering that only the conservative forces act in a generic unloading-reloading cycle. Consequently, the failure process stops in a generic unloading-reloading cycle, which is thereby characterized by constant values of A_{res}. In this case, the unloading-reloading behavior is governed by the material properties only. The average slope of the unloading-reloading cycle in the $\sigma_{eff} - \varepsilon_{eff}$ curve, $\tan\alpha_{eff}$ (Fig. 6), is therefore equal to the average slope of the unloading-reloading cycle in the $\bar{\sigma} - \bar{\varepsilon}$ curve, $\tan\alpha$, multiplied by the factor A_n/A_{res}, where A_{res} is the resistant area at the unloading point:

$$\tan\alpha_{eff} = \frac{A_n}{A_{res}}\tan\alpha. \tag{28}$$

In the $\sigma_{eff} - \varepsilon_{eff}$ curve, the average slope of the unloading-reloading cycle represents the effective stiffness at the unloading point. We assume that the effective stiffness at the unloading point is equal to E_s, the secant stiffness in the effective law:

$$E_s = \tan\alpha_{eff}. \tag{29}$$

Consequently, the generic point $\sigma_{eff} - \varepsilon_{eff}$ results from the intersection of the two lines $\sigma = \sigma_{eff}$ and $\sigma = E_s\varepsilon$ (Fig. 6). Imposing equality between the two effective stiffness (Eq. (29)), is equivalent to assuming that the effective behavior is elastic, and the (effective) strain is fully recovered after unloading.

1.3 Experimental validation of the identification procedure

For plotting purposes, note that Eq. (3) may be put in the form:

$$\frac{A_{res}}{A_n} + D = 1, \tag{30}$$

which means that the normalized resistant area, A_{res}/A_n, is given by the complement to 1 of the damage parameter, D, and the damage parameter is given by the complement to 1 of the normalized resistant area. Hence, the same plot provides both the normalized resistant area and the damage parameter, for any given value of $\bar{\varepsilon}$.
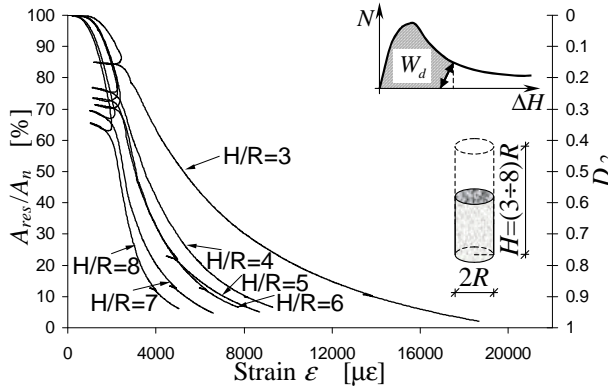
Figure 7: Normalized resistant area and D_2 damage law for variable slenderness

Fig. 7 shows the D_2 damage laws (values to be read on the right vertical axis) and related normalized resistant area laws (values to be read on the left vertical axis) for concrete cylinders with H/R ratios varying from 3 to 8. From Fig. 7 we can appreciate that the resistant area starts to decrease soon after the beginning of the testing and the damage process characterizes the entire duration of the test. The plots in Fig. 7 are size-effect sensitive. Indeed, the higher the H/R ratio, the higher is D_2 and the lower is A_{res} for any given value of $\bar{\varepsilon}$. For each plot, a flex point can be identified for a value of $\bar{\varepsilon}$ which approximately corresponds to $\hat{\varepsilon}$, defined in Eq. (10). Thus, the slope of the A_{res} law (and, consequently, of the D_2 law) reaches its maximum absolute value for $\varepsilon = \hat{\varepsilon}$. This validates the assumption of a non zero tangent of A_{res} (and, consequently, of D_2) for $\varepsilon = \hat{\varepsilon}$, an assumption which is at the basis of the analytical findings about the existence of strain-softening for $0 \leq \bar{\varepsilon} \leq \hat{\varepsilon}$

(§1.1):

$$\frac{dA_{res}(\bar{\varepsilon})}{d\bar{\varepsilon}}\bigg|_{\bar{\varepsilon}=\hat{\varepsilon}} \neq 0; \quad \frac{dD(\bar{\varepsilon})}{d\bar{\varepsilon}}\bigg|_{\bar{\varepsilon}=\hat{\varepsilon}} \neq 0. \tag{31}$$

As far as the existence of strain-softening for $\bar{\varepsilon} > \hat{\varepsilon}$ is concerned, the experimental evaluation of the damage parameter allows us to plot the function q, defined by Eq. (20). In Fig. 8, q is plotted in function of the displacement u. The plot of the function $q(\bar{\varepsilon})$ is homothetic to the relationship in Fig. 8. Since q turns out to be a positive-valued, monotone, strictly non-increasing function for $u > \hat{u}$ and, consequently, for $\bar{\varepsilon} > \hat{\varepsilon}$, it follows that:

$$\frac{dq(\bar{\varepsilon})}{d\bar{\varepsilon}} < 0 \quad \bar{\varepsilon} > \hat{\varepsilon}. \tag{32}$$
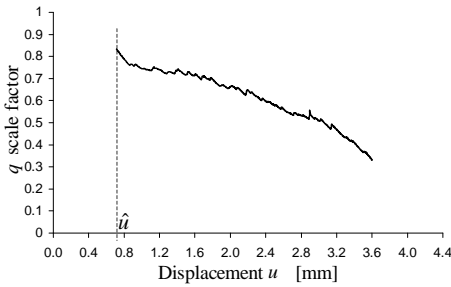
Figure 8: Scale factor between the percentage resistant area and normalized load laws
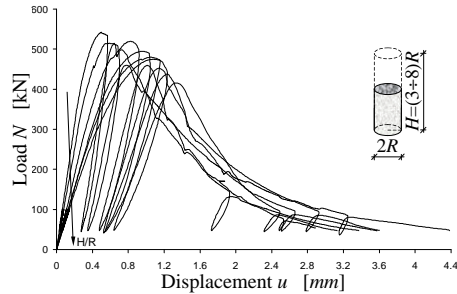

Figure 9: Size effect for the load-displacement diagrams

Eqs. (23) and (32) allow us to conclude that the effective law, $\sigma_{eff} - \varepsilon_{eff}$, is not strain-softening either in the $\bar{\varepsilon} > \hat{\varepsilon}$ range:

$$\frac{d\sigma_{eff}(\bar{\varepsilon})}{d\bar{\varepsilon}} > 0 \quad \bar{\varepsilon} > \hat{\varepsilon}. \tag{33}$$

The load–displacement diagrams, $N - u$, for the specimens with $H/R = 3 \div 8$ are shown in Fig. 9. They are clearly size-effect sensitive, with the tangent for $u = 0$ and the maximum load both decreasing with the increasing of the H/R ratio. The $\bar{\sigma} - \bar{\varepsilon}$ diagrams also turn out to be size-effect sensitive (Fig. 10), making it impossible to identify a unique law for the material.

Fig. 11 shows how the unloading law in the $\bar{\sigma} - \bar{\varepsilon}$ plane is clearly independent of the slenderness ratio of the specimen. This result supports the assumption whereby
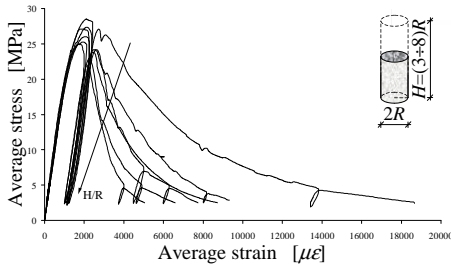
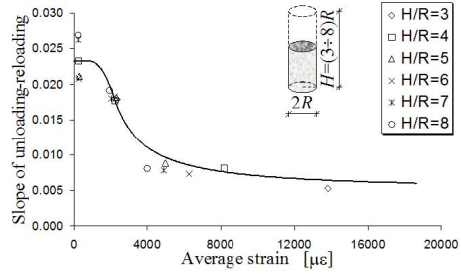Figure 10: Size effect for the average stress-average strain diagrams

Figure 11: Interpolating law of the average slope of the unloading-reloading cycles

all parameters characterizing the unloading-reloading cycles, included their average slope, are linked to proprieties of the material and do not depend upon the failure process affecting A_{res}. Therefore, this result can be considered as an indirect validation of the assumption whereby A_{res} does not change during the unloading-reloading cycles, which is at the basis of the identification procedure of the effective strain (§1.2). On the other hand, even Fig. 7 supports the same assumption, since the ratio A_{res}/A_n never decreases during an unloading-reloading cycle, on the contrary, A_{res}/A_n sometimes increases during unloading, due to the partial re-closure of the macro-crack and the subsequent possibility of transferring load between the two rough surfaces of the re-closed macro-crack. This leads a part of material isolated by the propagation of the macro-crack to interact with the inner resistant core until the unloading load is recovered, after reloading.
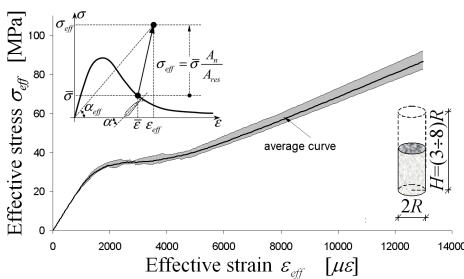

Figure 12: $\sigma_{eff} - \varepsilon_{eff}$ dispersion range for variable slenderness and average curve
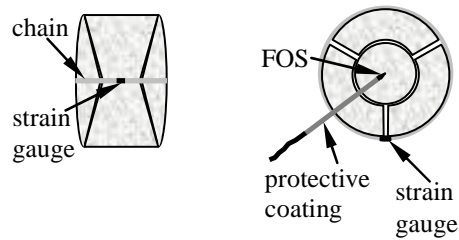

Figure 13: Strain-gauge for circumferential strain acquisition and FOS sensor for radial strain acquisition

The $\sigma_{eff} - \varepsilon_{eff}$ relationships obtained for the six geometries fall within the dispersion range in Fig. 12. The average curve in Fig. 12 is monotonically non-

decreasing, as was expected from the preventive analytical analysis (Eq. (33)). It is worth noting that the monotonicity of the effective law was not assumed a-priori, but was obtained directly from experimental data, scaling the applied load by the experimentally evaluated resistant area.

As previously anticipated, one of the main consequences of the model of the inner resistant core concerns the behavior of Poisson's ratio and volumetric strain during the uniaxial compression test. As a matter of fact, if the propagation of the macro-crack isolates the outer part of the specimen causing it to lose its capability of carrying load, while the inner core (which is biconic in cylinders) represents the resistant structure of the specimen, it seems more reasonable to acquire strains within the inner resistant core instead of on the surface of the specimen. The acquisition of a strain along the circumference of the middle cross-section (by means of the strain-gauge in Fig. 13, for example), ε_c, has often been used in order to evaluate the radial strain, ε_r, since ε_r and ε_c have the same value in cylinders:

$$\varepsilon_r = \frac{\Delta R}{R} = \frac{2\pi\Delta R}{2\pi R} = \frac{\Delta(2\pi R)}{2\pi R} = \frac{\Delta crf}{crf} = \varepsilon_c, \tag{34}$$

where crf stands for "circumference". The value of ε_r evaluated by means of Eq. (34), may then be used for estimating Poisson's ratio, ν, defined as:

$$\nu = -\frac{\varepsilon_r}{\varepsilon_l}, \tag{35}$$

where ε_l is the longitudinal strain given by Eq. (7):

$$\varepsilon_l = \bar{\varepsilon} = \frac{\Delta H}{H}. \tag{36}$$

This gives rise to the $\varepsilon_r/\varepsilon_l$ plot in Fig. 14, giving a Poisson's ratio that rapidly reaches non-physical values greater than 0.5. The reason for this is that Eq. (34) does not provide a strain, since the last equality is only valid until the crack starts to propagate. As the crack propagates throughout the test (see damage laws in Fig. 7), the variation of the circumference length is due, in part, to material deformation and, in part, to the space between the two surfaces of the opening crack. Thus, Eq. (34) cannot be employed to evaluate Poisson's ratio.

By acquiring the radial strain inside the inner core (using the FOS sensor in Fig. 13, for example) we find a $\varepsilon_r/\varepsilon_l$ ratio almost independent of ε_l. This means that Poisson's ratio is almost independent of the loading step, which is physically expectable since Poisson's ratio is a constitutive property, that is, a property related to the material only.
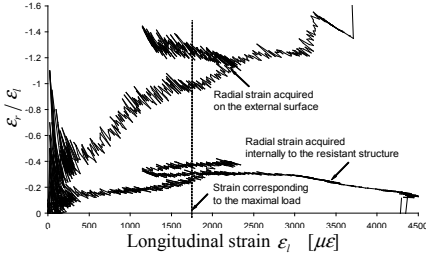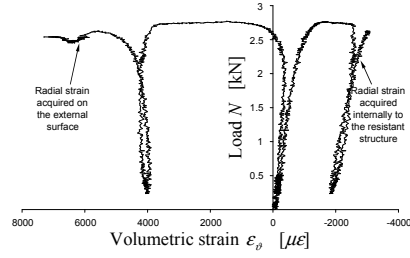
Figure 14: Traditional and identified $\varepsilon_r/\varepsilon_l$ ratios

Figure 15: Traditional and identified volume curves

The volumetric strain, ε_ϑ, is the ratio of the change in the volume of a body, which occurs when the body is placed under pressure, to the original volume of the body:

$$\varepsilon_\vartheta = \frac{\Delta V}{V}. \tag{37}$$

ε_ϑ is equal to the first invariant of strain, $I_{1\varepsilon}$, which is the trace of the strain tensor:

$$I_{1\varepsilon} = \varepsilon_1 + \varepsilon_2 + \varepsilon_3, \tag{38}$$

where ε_1, ε_2, and ε_3 are the principal strains. In cylindrical specimens, the principal strains are equal to ε_l, ε_r, and ε_c, with $\varepsilon_r = \varepsilon_c$. Thus, in cylinders ε_ϑ is bonded to ε_l and ε_r as follows:

$$\varepsilon_\vartheta = I_{1\varepsilon} = \varepsilon_l + \varepsilon_r + \varepsilon_c = \varepsilon_l + 2\varepsilon_r. \tag{39}$$

Assuming ε_r given by Eq. (34), the volumetric curve, $N - \varepsilon_\vartheta$, proves to be mostly in the positive field (Fig. 15). This involves the increase in volume of the specimen under pressure and is known as dilatancy. On the contrary, using the radial strain acquired internally to the resistant core, the volumetric curve is in the negative field (Fig. 15). Hence, it appears that there is no real increase in the volume of a concrete solid when the solid is placed under pressure.

1.4 Numerical validation of the identification procedure

We have already discussed (§1) the possibility of using a local law, such as the effective law, for modeling nonlocal effects. Here, we will show some numerical results given by a Cell Method (CM) code using the effective law as constitutive law.
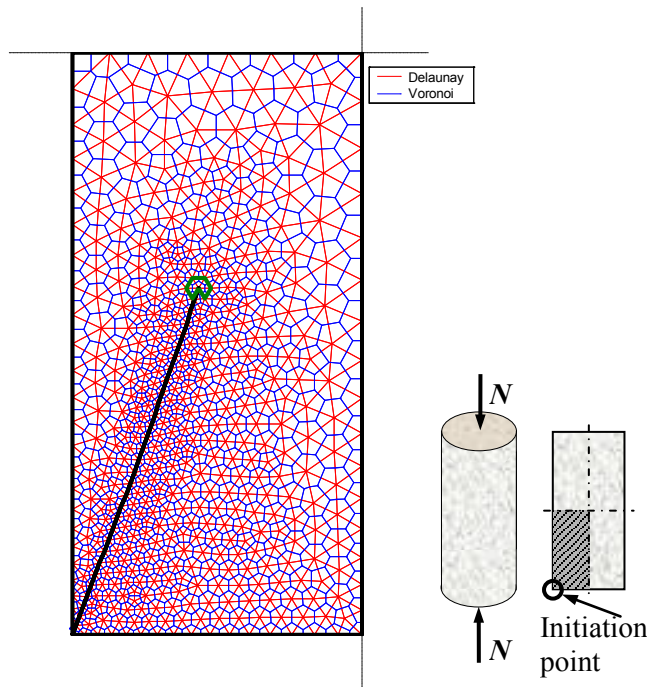
Figure 16: Crack path for the bottom-left quarter of the longitudinal section

Fig. 16 shows the crack path identified by the model for a uniaxial compressed cylindrical specimen, where the direction of propagation is computed step by step, taking into account the modification of the stress field induced by the previous crack propagation. The average slope of the crack path in Fig. 16 is approximately 70° and reflects the values observed experimentally (Fig. 1) in the cylinders used for identifying the effective law to be applied for the modeling (Fig. 12).

The code operates in displacement control, identifying the crack length for each increment of relative displacement given between the platens of the test machine and computing the external load. The crack length and the external load at each displacement increment depend upon the H/R ratio. The numerical $\bar{\sigma} - \bar{\varepsilon}$ curves given in Fig. 17 for the 6 tested geometries accord well with the experimental values (Fig. 10). In particular, it is worth noting how the $\bar{\sigma} - \bar{\varepsilon}$ curves are strain-softening even if the constitutive law being used, the effective law in Fig. 12, is monotonically non-decreasing. This happens because the crack propagation causes a part of the longitudinal section to unload, reducing the resistant area at each propagation, and, as a consequence, a smaller resistant area involves a smaller carried load for any
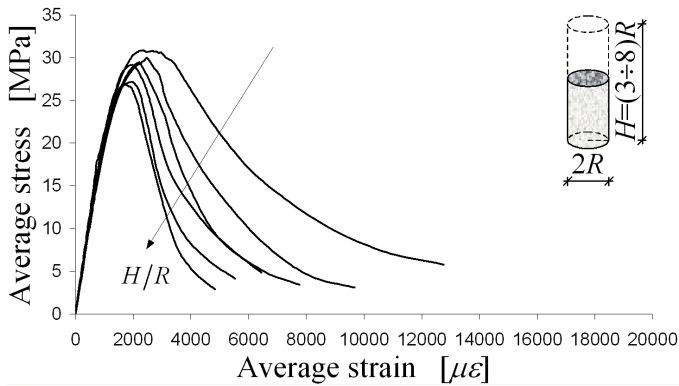
Figure 17: Numerically evaluated size-effect on average stress-average strain diagrams
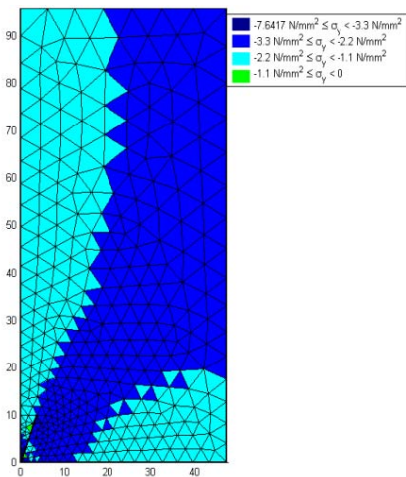

Figure 18: Axial stress analysis on the longitudinal section for plain concrete
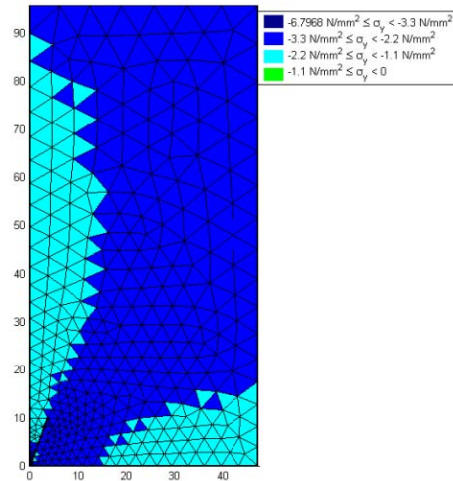

Figure 19: Axial stress analysis on the longitudinal section for wrapped specimen

given relative displacement between the platens of the test machine. Fig. 18 shows the axial stress field on the longitudinal section for a short crack propagation (the crack tip is located at about 10 *cm* from the lower platen). Two effects on the stress field are clearly visible in Fig. 18: the first is given by the constraint provided by the lower platen, since we have assumed no sliding (perfect adherence) between the specimen and the platen itself, and the second is the unloading of the material lying between the crack and the external surface, which also causes unloading of

the above material, significantly decreasing the resistant area of the specimen.

A further numerical result showing how the local effective law may provide nonlocal analysis concerns the modeling of the compression test for concrete cylinders wrapped with FRP sheets. The stress field in Fig. 19 shows how the external wrapping counteracts the stress unloading induced by crack propagation. In particular, the comparison between Figs. 18 and 19 allows a direct estimation of how much the external wrapping modifies the stress field along the longitudinal section, since the crack length is the same in both figures. This results in a greater resistant area for FRP wrapped cylinders, for the same crack length. As a consequence, the difference between material and specimen behavior is lower, that is, the difference between the plot of the $\sigma_{eff} - \varepsilon_{eff}$ and $N - u$ laws is lower. This analysis leads to the conclusion that the well-known disappearance of the softening branch in the $N - u$ laws of FRP wrapped specimens should not be associated with the high Young's modulus for the wrapping, as usually assumed, but with a resistant area that is closer to the nominal area than in plain concrete: for a number of FRP sheets sufficient to make the difference between A_n and A_{res} negligible, the specimen behavior proves to be monotonically non-decreasing, as does the effective law.
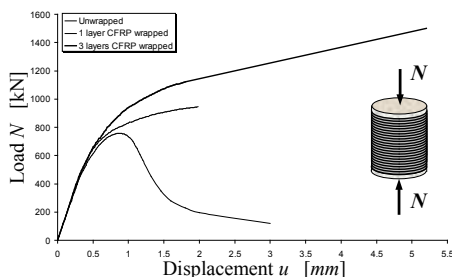

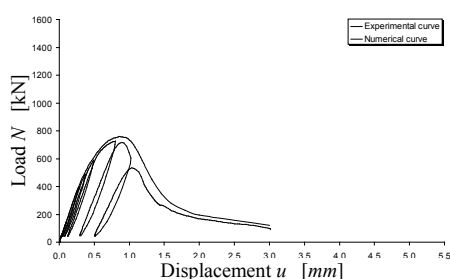Figure 20: Numerical load-displacement curves for unwrapped and CFRP wrapped specimens

Figure 21: Numerical and experimental results for the unwrapped specimens

The numerical $N - u$ curves given by varying the number of FRP sheets only (without modifying the constitutive law, which is the effective law) are shown in Fig. 20. They are compared with the experimental $N - u$ curves in Figs. 21-23.

The different speed of the A_{res} decrement during the compression test could also explain the shape-effect in brittle materials (see Fig. 24 for marble), which involves no softening branch in the $N - u$ ($\bar{\sigma} - \bar{\varepsilon}$) curves for small slenderness ratios, $H/(2R)$, and a softening becoming increasingly prominent as the $H/(2R)$ ratio increases. Actually, as initially pointed out by Hudson Brown and Fairhurst (1971), smaller
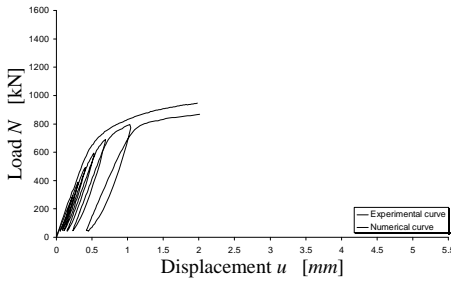
Figure 22: Numerical and experimental results for the one-layer CFRP wrapped specimens
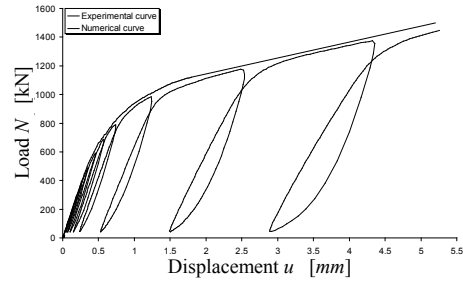
Figure 23: Numerical and experimental results for the three-layer CFRP wrapped specimens

$H/(2R)$ ratios involves a smaller decrement of A_{res} and, consequently, a $\bar{\sigma} - \bar{\varepsilon}$ curve closer to the monotonically non-decreasing $\sigma_{eff} - \varepsilon_{eff}$ curve (see Figs. 25-26, where F is the external load N and A_0 stands for A_n, $A(\varepsilon)$ for A_{res}, σ_0 for $\bar{\sigma}$, σ_{TRUE} for σ_{eff}).

Fig. 17, previously discussed, also shows how the CM code is able to capture the shape-effect for a small variation range of the $H/(2R)$ ratio.

2   Experimental program

One peculiar aspect of the shape-effect is the different behavior, in terms of load-displacement diagrams, between cubic and cylindrical concrete specimens. That is, the shape of the $N - u$ diagrams is different in cylinders than in cubes. Consequently, the shape of the $\bar{\sigma} - \bar{\varepsilon}$ diagrams is also different in cylinders than in cubes (Fig. 27). In particular, as well known, the cylinder strength is between 5% and 25% less than the cube strength, the percentage difference decreasing with an increase in the concrete strength. Also, a decrease in either the size or the aspect ratio of specimens leads to a decrease in the ratio of standard cube strength to that of other specimens.

Usually, the concrete technology tests the conformity of compressive strength on cubes with a size of 150 *mm*, after 28 days, which were mix cured (first 7 days under water, remaining 21 days exposed to air). Then, a factor of 0.83 (BS 1881: Part 120) is introduced to convert cube to cylinder strength for normal strength concrete. According to the concrete standard MSZ EN 206-1:2002, the conversion factor between the strength of cubic specimens with a size of 150 *mm* and the strength of cylindrical specimens with a 150 *mm* diameter and 300 *mm* height must be changed into 0.76/0.97 when the specimens are wet cured.
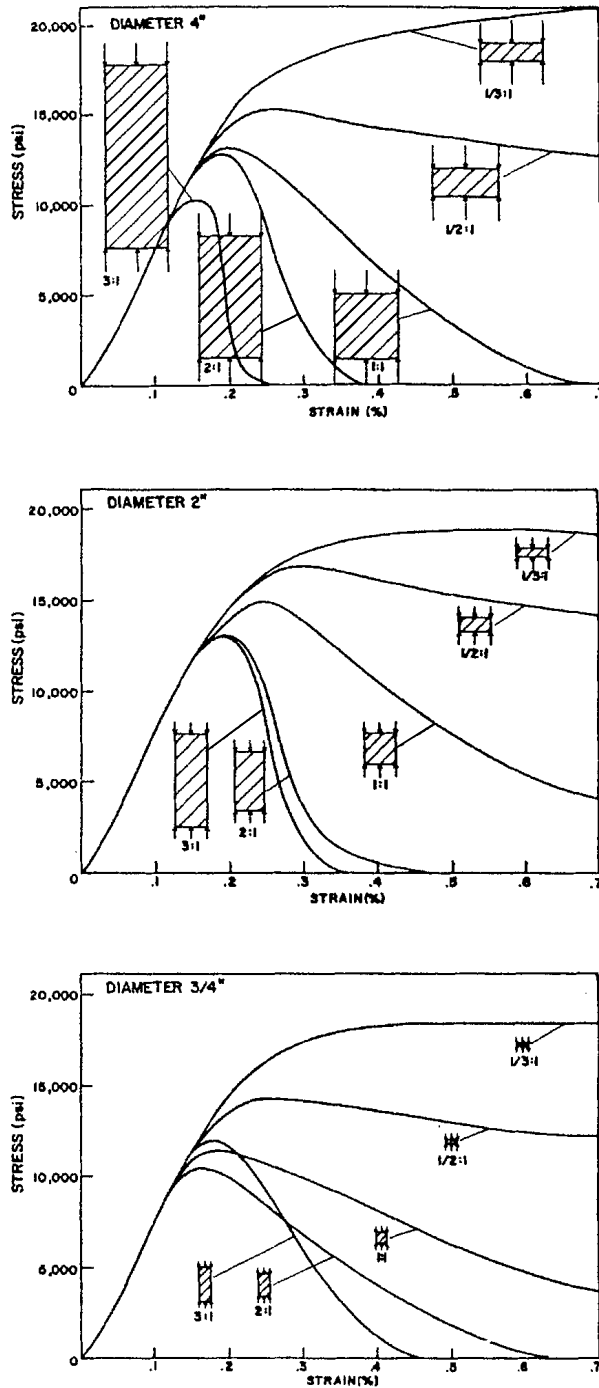
Figure 24: Influence of specimen shape on the $\bar{\sigma} - \bar{\varepsilon}$ curve for marble loaded in uniaxial compression [Hudson Brown and Fairhurst (1971)]
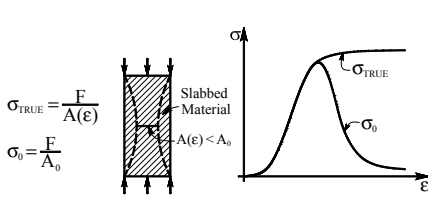
Figure 25: Effect of stress definition on the shape of the stress-strain curve for large $H/(2R)$ ratio [Hudson Brown and Fairhurst (1971)]
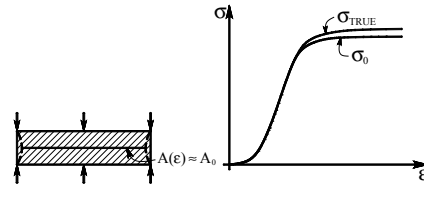
Figure 26: Effect of stress definition on the shape of the stress-strain curve for small $H/(2R)$ ratio [Hudson Brown and Fairhurst (1971)]
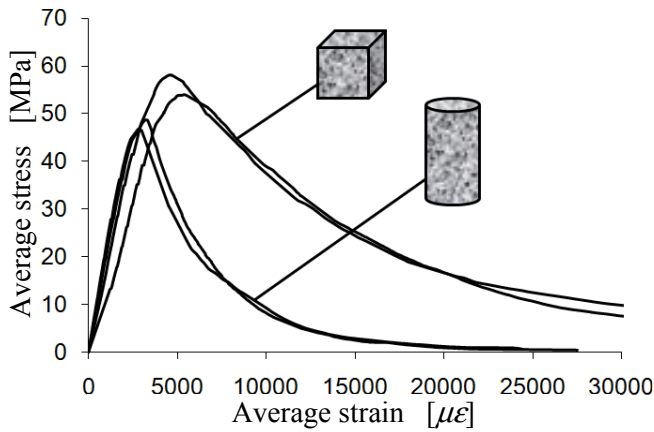
Figure 27: Shape-effect for cubic and cylindrical concrete specimens

Since the compressive strength is calculated by dividing the maximum load by the nominal area, A_n, the idea at the basis of the present experimentation is to verify whether or not the difference between cylinder and cube strength vanishes when the resistant area, A_{res}, is substituted for A_n. This verification of the actual constitutive nature of the effective law was carried out for two different mixtures, one of plain concrete and the other of rubberized concrete [Ferretti and Bignozzi (2011); Ferretti and Bignozzi (2012)], obtained by substituting a part of the fine aggregate with rubber scraps (Fig. 28) produced by grinding discarded tires (PFU scraps). The composition of the PFU scraps used in the experimentation is shown in Tab. 1.

Usually, concrete rubberization is used as a technique for recycling waste tires, joining all the previous techniques for recycling waste tires, thereby giving rise

Figure 28: Gommamica Powerfill ECO (SBR Styrene Butadiene Rubber) rubber coarse aggregate, commercialized by Elastrade Srl

Table 1: Composition of the PFU scraps

COMPONENTS	Weight%
Rubber (hydrocarbon)	50-55
Lampblack	26-30
Acetone	9-13
Ashes	6-8
Sulfur	1-3

to a wide range of non-structural elements. Recently, concrete rubberization was shown to be able to produce a mixture that could also be employed for structural purposes [Ferretti and Bignozzi (2012); Ferretti (2012a)], as a result of an experimental programme that has provided the opportunity of reviewing the classical solution of Boussinesq's problem for a homogeneous linear-elastic and isotropic half-space subjected to a point-load [Ferretti (2012b)].

2.1 Mixtures and specimens preparation

Experimentation was carried out at the LISG-RM laboratory of the Engineering Faculty of the University of Bologna, Department of Civil, Environmental and Materials Engineering (DICAM).

The two concrete mixtures used in the experimentation share the same type of binder (Portland II AL 45.5R Micronmineral), alluvial coarse aggregates ($8 - 15$ *mm*) and fine aggregates (sand of $0 - 5$ *mm* and River Po sand of $0 - 2$ *mm*). In addition, a $1 - 2.4$ *mm* rubber aggregate was used for the rubberized mixture (Fig. 28).

Table 2: Weight composition and W/C ratio of Mixture 1

COMPONENTS	kg/m^3	Weight%
River Po sand	124.0	5.4
Sand	725.5	31.3
Coarse aggregates	916.2	39.6
Cement	359.2	15.5
Water	188.7	8.1
Admixture	2.4	0.1
Total	2316.0	100.0

W/C	0.52

Table 3: Weight composition and W/C ratio of Mixture 2

COMPONENTS	kg/m^3	Weight%
River Po sand	130.7	6.6
Sand	493.8	24.7
Coarse aggregates	794.1	39.8
PFU scraps	87.7	4.4
Cement	328.0	16.4
Water	159.8	8.0
Admixture	2.6	0.1
Total	1996.7	100.0

W/C	0.48

The two mixtures were designed to reach super fluid consistency, class S5 consistency (Italian standards UNI EN 206-1:2006 and UNI 11104:2004). Since a considerable amount of water is required to reach super fluid consistency, leading to a decrease in strength and resistance to frost and aggressive environments in hardened concrete and to an increased danger of segregation and bleeding, we used a polyacrylic superplasticizer admixture (Axim Creactive LX fluxing agent) to ensure that the quantity of water utilized was not excessive.

In this paper, the plain and the rubberized mixture will be called Mixture 1 and Mixture 2, respectively. The compositions of the two mixtures and their water/cement ratios, W/C, are shown in Tabs. 2 and 3.

Figure 29: Laboratory batch mixer

Figure 30: Preparation of the specimens

Coarse and fine natural aggregates and rubber aggregates (for Mixture 2 only) were fed into the concrete mixer in that order (Fig. 29) and mixed for 5 mins. The cement was then added and mixed with aggregates for a further 2 mins. Finally, 75% of the water and the admixture with the remaining water were added and mixed for 10 mins.

In order to derive qualitative information only about the sensitiveness of the effective law to the shape-effect, only two specimens were tested for each shape-mixture combination. This meets the requirement whereby at least two standard-cured specimens made from the same concrete sample must be tested at the same age. In conclusion, the tested specimens are: two Mixture 1 cubes, two Mixture 1 cylinders, two Mixture 2 cubes, and two Mixture 2 cylinders.

A further requirement concerns the specimen's dimensions, as the cylinder's diameter and the cube's edge should be at least 3 times the nominal maximum size of the coarse aggregate used in the concrete. Moreover, the ASTM Standard for a test cylindrical specimen is about 150 *mm* (5.9 inches) ×300 *mm* (diameter) (11.8 inches)

(high). Our cubic specimens are 150 *mm* square and the cylindrical specimens are 150 *mm* in diameter and 300 *mm* in height.

The concrete was poured into the cubic and cylindrical molds in layers approximately 5 *cm* thick and tempered properly (UNI EN 12350-1 and UNI EN 12390-1) to eliminate any voids (Fig. 30). Each layer was compacted using a tamping rod (hemispheric-nosed steel rod 16 *mm* diameter and 60 *cm* length, bullet pointed at lower end) and not less than 35 strokes per layer. The rodding was distributed evenly over the specimen area, taking care to penetrate slightly into the previous layer when packing the second and/or following layers. Finally, the top surface was leveled and smoothed over with a trowel.

Figure 31: Curing room under controlled thermo-hygrometric conditions

Figure 32: Automatic cylinder-end grinder

The test specimens were stored in moist air for 24 hours. After this period, the specimens were marked and removed from the molds. According to the UNI EN 12390-2 specifications, all specimens prepared from each batch of concrete were cured under identical conditions in a curing room (Fig. 31), before testing them at the same age.

According to UNI EN 12390-1 specifications, to provide a uniform load distribution when testing, the ends of the specimen should be perpendicular to the cylinder axis, with a tolerance of $0.5°$, and they should be plane to within 0.05 *mm* (0.002 *inches*). To achieve this, we ground the ends of cylindrical specimens using an automatic grinder provided with a diamond cutting wheel with a 800 mm diameter (Fig. 32), whilst grinding was not necessary for the cubes, since these need only to be placed in the testing-machine in such a way to ensure that the load is applied to the opposite sides of the cube cast. End-grinding allows compression testing to start immediately, without using capping materials. This eliminates the fumes and

waiting time associated with capping the compound.

Figure 33: Analogical centesimal comparator and carpenter's square for checking planeness and perpendicularity

Figure 34: Hot glue gun loaded with a glue stick and probes for microseismic analysis: the red probe is the transmitting sensor, while the green probe is the receiving sensor

After grinding the cylinders, planeness was checked using a straight-edge and a feeler gauge with an acquisition range of between 0.025 and 0.254 mm (0.001 and 0.010 in.) (see Fig. 33 for the feeler gauge, which is an analogical centesimal comparator), taking a minimum of three measurements on different diameters, while the perpendicularity was checked using a carpenter's square with one arm longer than the specimen to be tested, the 90-degree angle accurate within 0.1 degree, and the outer edges machined straight within 0.025 mm (0.001 ins.) along their entire length (Fig. 33). In both cases, the specimen end was positioned over a suitable metal plate (Fig. 33) placed on a bench and leveled up so that it was horizontal.

Cubic and cylindrical specimens were instrumented with two probes for microseismic analysis (Fig. 34) and two LVDTs (Linear Variable Displacement Transducers), which are inductive displacement transducers (Fig. 35).

The microseismic probes were attached to the cleaned specimen surface, on the middle-height cross-section (Fig. 35), by means of hot glue (Fig. 34). For the cubic specimens, the gluing points are the central points of the two sides of the cube cast opposite to the loaded sides. Gluing the microseismic probes is a manual operation that needs to be carried out very quickly, when the glue applied to the specimen is still liquid, so that the film of glue between the probes and the specimen is as thin as possible, to avoid the inclusion of air bubbles. This will ensure that a good microseismic signal can be received by the receiving sensor.

Figure 35: Positioning of the instrumented cylindrical specimen on the compression-testing machine

Figure 36: Compression-testing machine and acquisition apparatus

The lower plate of the compression-testing machine is provided with concentric circular marks (Fig. 35), for centering purposes. Cylindrical specimens were centered on the lower plate by using the centering marks. A circular metal plate 4 cm (1.57 ins.) thick and 28.4 cm (11.18 ins.) in diameter was placed on the lower plate (Fig. 36) when testing cubic specimens, in order to space the two plates as far as needed to locate the two LVDT transducers, since the height of the magnetic support of the two LVDT transducers is greater than the specimen size. The flat surfaces of the circular plate are plane with a tolerance of not more than ±0.013 mm (0.0005 ins.) and are parallel to within 0.05 degrees. The sides of the metal plate are engraved with eight equally spaced lines perpendicular to the flat ends, while the flat ends are engraved with concentric circular marks, in both cases for centering purposes. The metal plate was centered on the lower plate of the compression-testing machine by using the eight equispaced lines and the cubic specimens were centered using the centering marks engraved on the flat ends.

The two LVDT transducers were fixed to a magnetic support (Fig. 35) and positioned along one diameter of the circular marks engraved on the lower plate (Fig. 35), at an equal distance from the plate center. The displacement u giving the average vertical strain $\bar{\varepsilon}$ according to Eq. (7) has been evaluated as the average displacement provided by the two LVDTs.

The compression tests were performed in accordance to the technical standard UNI EN 12390-3. The loading rate of the hydraulic machine was maintained in a range between 0.15 and 0.35 MPa/s (20 to 50 psi/s), as required, during the latter half of the loading phase.

2.2 Results on plain concrete

The acquired load displacement relationships, $N - u$, and the related average stress-average strain relationships, $\bar{\sigma} - \bar{\varepsilon}$, for plain concrete are shown in Figs. 37 and 38, respectively, where the compressive stresses and strains are positive.
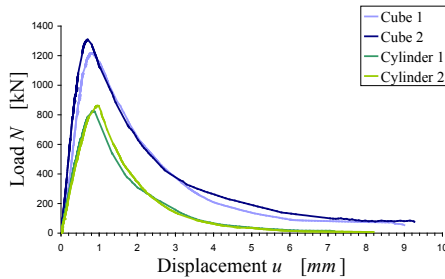

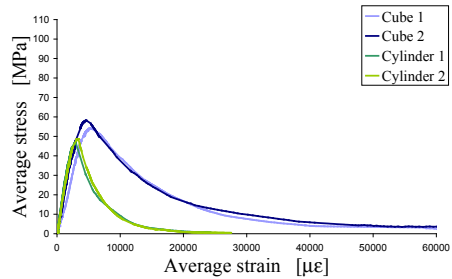Figure 37: Load-displacement diagrams for Mixture 1

Figure 38: Shape-effect on the average stress-average strain diagrams for Mixture 1
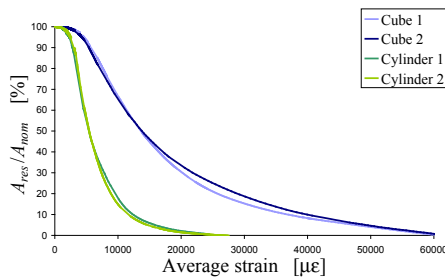
Figure 39: Shape-effect on the decrement of resistant area for Mixture 1
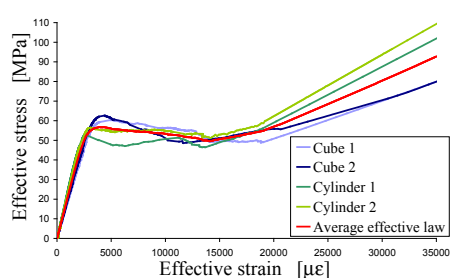
Figure 40: Effective stress-effective strain diagrams for cubic and cylindrical specimens and average effective law for Mixture 1

As can be easily observed in both Figs. 37 and 38, specimens of the same geometry give almost the same results, while the shape-effect between cubic and cylindrical specimens is clearly evident, leading to a maximum load for cylinders that is 15% lower than the maximum load for cubes (Fig. 38). Moreover, the post-peak branch of the $\bar{\sigma} - \bar{\varepsilon}$ relationships in cubic specimens is very far from the post-peak branch in cylindrical specimens.

Applying the identification procedure of the effective law to the tested specimens, we found that the law describing the resistant area is sensitive to the specimen's shape, leading to an A_{res} decrement faster in cylinders than in cubes (Fig. 39), with A_{res} computed, according to Eqs. (3) and (7), as:

$$A_{res} = A_{res}(\bar{\varepsilon}) = A_n(1 - D(\bar{\varepsilon})), \tag{40}$$

where D is the microseismic damage parameter defined in Eq. (25). Consequently, the ratio between cubic effective strength and cylindrical effective strength, $\sigma_{eff_{\max}}/\varepsilon_{eff_{\max}}$, is different to the ratio between cubic strength and cylindrical strength, $\bar{\sigma}_{\max}/\bar{\varepsilon}_{\max}$, where σ_{eff} is computed according to Eq. (8) and ε_{eff} is identified following the scheme set out in Fig. 6.

The effective laws identified for cubic and cylindrical specimens are shown in Fig. 40, together with the average effective law for the four plain concrete specimens. As can be seen in Fig. 40, no shape-effect seems to characterize the effective law for plain concrete, since the effective laws for cubic specimens intersect the effective laws for cylindrical specimens in a random manner. Moreover, even in this experimentation, the softening branch disappears in the effective law and is substituted by two branches, the first approximately horizontal and the second hardening.

The apparent high difference between the average hardening slopes of cubes and cylinders cannot be related to a shape-effect for high strains, due to the low number of tested specimens and the experimental uncertainties that characterize data acquisition in the last part of the compression test. Fig. 40 only allows us to state that a final almost linear hardening branch exists in the effective law of plain concrete, both for cubes and cylinders. The slope of this final branch must be investigated by means of further experimentation.

For quantitative purposes, with the aim of deriving the effective characteristic strength for cubes, $\sigma_{ck,\,eff_{cub}}$, and cylinders, $\sigma_{ck,\,eff_{cyl}}$, of course, many more than two compression tests are required for each shape (we estimate 100 compression tests). Nevertheless, Fig. 40 allows us to assume that the effective laws for cubes and cylinders will intersect in a random manner in all cases. Consequently, taking as the effective characteristic strength, $\sigma_{ck,\,eff}$, the average effective strength in the approximated horizontal branch, to be on the safe side, we find:

$$\sigma_{ck,\,eff_{cub}} \cong \sigma_{ck,\,eff_{cyl}}. \tag{41}$$

2.3   Results on rubberized concrete

The acquired load displacement relationships, $N - u$, for rubberized concrete are shown in Fig. 41. From the comparison between Figs. 37 and 41, we can appreciate

how rubber aggregates involve a decrement of maximum load in both the cubic and the cylindrical specimens.

Figure 41: Load-displacement diagrams for Mixture 2
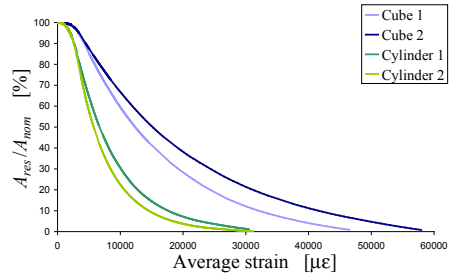
Figure 42: Shape-effect on the decrement of resistant area for Mixture 2

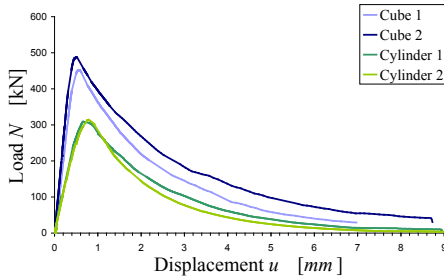As for plain concrete, the $N - u$ relationships in Fig. 41 lead, by changing the scale, to $\bar{\sigma} - \bar{\varepsilon}$ relationships that exhibit an evident shape-effect between cubic and cylindrical specimens, resulting in a maximum load for cylinders that is 16% lower than the maximum load for cubes. Even in this case, however, the law describing A_{res} is sensitive to the specimen shape, providing an A_{res} decrement faster in cylinders than in cubes (Fig. 42). Once more, this leads to effective laws that do not exhibit any shape-effect (Fig. 43), with an effective characteristic strength for cubes, $\sigma_{ck,\,eff_{cub}}$, comparable to the effective characteristic strength for cylinders, $\sigma_{ck,\,eff_{cyl}}$.

Figure 43: Effective stress-effective strain diagrams for cubic and cylindrical specimens and average effective law for Mixture 2

Figure 44: Design stress-strain diagram for concrete

3 New design relationships

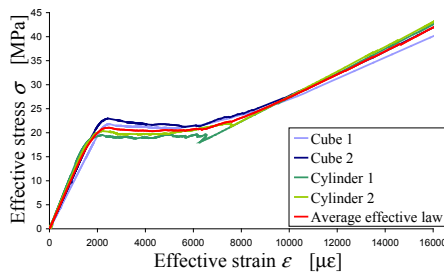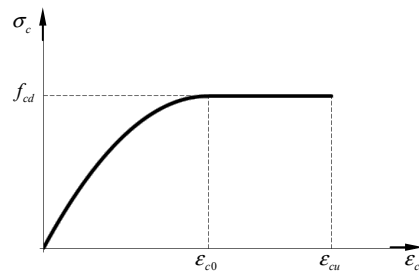As can be seen in Figs. 40 and 43, if we neglect the hardening branches (to be on the safe side) the average effective laws resemble the design relationship between concrete stress, σ_c, and concrete strain, ε_c, used in the semi-probabilistic limit state design method (Fig. 44).

The design relationship is composed of two branches, the first parabolic and the second horizontal. Due to its shape, the design relationship is also called the parabola-rectangle stress-strain diagram.

In Fig. 44, the compressive stresses and strains are assumed to be positive. In particular, the strain at the end of the parabolic branch assumes the conventional value ε_{c0}, equal to:

$$\varepsilon_{c0} = 2\%_0, \tag{42}$$

and the ultimate strain, ε_{cu}, is equal to:

$$\varepsilon_{cu} = 3.5\%_0. \tag{43}$$

Moreover, the cylindrical design strength f_{cd} is given by:

$$f_{cd} = \frac{0.85 f_{ck}}{\gamma_c}. \tag{44}$$

where:

- f_{ck} is the cylindrical characteristic strength, closer to the in-situ characteristic strength than the cubic characteristic strength, R_{ck}, which is the experimentally evaluated strength (on cubic specimens) and is related to f_{ck} by means of the conversion factor 0.83:

$$f_{ck} = 0.83 R_{ck} \text{ for } \frac{H}{D} \geq 2. \tag{45}$$

  R_{ck} is defined as the lower fractile of order p (or the $p\%$ lower fractile), that is, the cubic strength having the $p\%$ probability of not being exceeded. It is derived from the experimental strengths, R_{ci}, $i = 1, 2, ..., n$, given by the n performed compression tests on cubic specimens, as:

$$R_{ck} = R_{cm} - k\delta, \tag{46}$$

  where, for $p = 5$, as usually assumed, k is equal to:

$$k = 1.645, \tag{47}$$

and R_{cm} and δ are, respectively, the average value:

$$R_{cm} = \frac{1}{n} \sum_{i=1}^{n} R_{ci}, \tag{48}$$

and the mean square error of the Gaussian distribution approximating the statistics of the experimental strength, R_c, which is a discrete random variable, when the number of performed tests is very high ($n \geq 100$):

$$\delta = \sqrt{\frac{\sum\limits_{i=1}^{n} (R_{ci} - R_{cm})^2}{n-1}}. \tag{49}$$

- The coefficient 0.85 takes into account the difference between the duration of the laboratory tests (short duration) and the application duration of real loads (long duration).

- γ_c is a factor of safety, which, for ultimate loads, is equal to (DM 14/01/2008):

$$\gamma_c = 1.5. \tag{50}$$

For $10 \leq n < 100$, the statistics of R_c can be still approximated to a Gaussian distribution, but the value of k in Eq. (47) must be changed according to the number of performed tests and the desired degree of confidence. Tab. 4 presents the values of k for $10 \leq n \leq 30$ and a confidence degree of 90% [La Tegola (1977)].

Table 4: Adjustment of the coefficient k for $10 \leq n \leq 30$ (90% confidence degree)

n	k
10	2.14
12	2.07
14	2.02
16	1.98
18	1.95
20	1.93
23	1.90
26	1.88
30	1.85

If a lower number of performed tests is available ($n < 10$), the Gaussian distribution is no longer adequate for describing the statistics of R_c. Consequently, Eq. (46) can no longer be employed for estimating R_{ck}.

Standards are more restrictive for the Italian regulations UNI EN 13791:2008 and DM 14/01/2008, and they state that the statistical approach must be abandoned whenever $n < 15$. If this is the case, Eq. (46) must be substituted by the following relationship giving the in-situ evaluation of R_{ck} when at least 3 tests have been performed on core samples:

$$R_{ck} = \frac{1}{0.83} \min\{f_{cm} - \bar{k}; \ f_{c,lowest} + 4\}, \tag{51}$$

where all strengths are expressed in N/mm^2, f_{cm} is the average cylindrical strength, $f_{c,lowest}$ is the lower cylindrical strength, and $\bar{k} = \bar{k}(n)$ depends on n according to Tab. 5.

Table 5: Relationship between $\bar{k}$ and n, for $3 \leq n < 15$ (UNI EN 13791:2008 and DM 14/01/2008)

n	$\bar{k} \ [N/mm^2]$
3-6	7
7-9	6
10-14	5

For $n \geq 15$, UNI EN 13791:2008 and DM 14/01/2008 give the in-situ R_{ck}, evaluated on the core samples, as:

$$R_{ck} = \frac{1}{0.83} \min\{f_{cm} - k\delta; \ f_{c,lowest} + 4\}, \tag{52}$$

where the mean square error, δ, must satisfy the condition:

$$\delta \geq 2 \, N/mm^2, \tag{53}$$

and, for $n = 15$ or in absence of further prescriptions:

$$k = 1.48. \tag{54}$$

By substituting Eqs. (45) and (50) into Eq. (44), we finally obtain the relationship between f_{cd} and R_{ck}, for $H/D \geq 2$:

$$f_{cd} = \frac{0.85 \cdot 0.83 R_{ck}}{1.5} = 0.47 R_{ck}. \tag{55}$$

It is now worth remembering that the design relationship in Fig. 44 has no experimental foundation: it is just a numerical relationship that has been shown to fit

the structural behavior well if used in numerical modeling. The identification procedure of the effective law allows us for the first time to derive an experimentally founded relationship that has the same shape of the design relationship.

In this section, we will use the identified effective laws to verify the reliability of the design relationship for plain concrete. The identified effective laws will be also used for proposing a design relationship for rubberized concrete, for which no technical standard has yet been formulated.

3.1 Plain concrete

According to DM 14/01/2008, the parabolic branch of the design relationship is given by the second-order function:

$$\sigma_c = 1000 f_{cd} \left(\varepsilon_c - 250 \varepsilon_c^2 \right) \quad \varepsilon_c \leq 2\text{‰}. \tag{56}$$

where f_{cd} is expressed by Eq. (44), whilst the second branch is given by the function:

$$\sigma_c = f_{cd} \quad 2\text{‰} < \varepsilon_c \leq 3.5\text{‰}. \tag{57}$$

So that the design relationship of Mixture 1 can be plotted, the value of R_{ck} must be known, in order to derive f_{cd} using Eq. (55). Since $n < 15$, the statistical approach cannot be used and R_{ck} must be derived from Eq. (51). The two cubic strengths, R_{c1} and R_{c2}:

$$R_{c1} = 54.06 \, N/mm^2, \tag{58}$$

$$R_{c2} = 58.08 \, N/mm^2, \tag{59}$$

can be converted into cylindrical strengths, f_{c1} and f_{c2} (Tab. 6), by means of the conversion factor 0.83, and used together with the cylindrical strengths f_{c3} and f_{c4} of the two cylindrical specimens for evaluating f_{cm} and $f_{c,lowest}$. Since a total of $n = 4$ cylindrical strengths are therefore available (Tab. 6), the parameter $\bar{k}$ given by Tab. 5 is:

$$\bar{k} = 7. \tag{60}$$

Table 6: Cylindrical strengths for the evaluation of R_{ck}

$f_{c1} \; [N/mm^2]$	$f_{c2} \; [N/mm^2]$	$f_{c3} \; [N/mm^2]$	$f_{c4} \; [N/mm^2]$
44.87	48.21	46.65	48.70

The result is:

$$R_{ck} = 48.32 \ N/mm^2, \tag{61}$$

which, substituted into Eq. (55), provides a value of design cylindrical strength equal to:

$$f_{cd} = 22.73 \ N/mm^2. \tag{62}$$

As far as the opportunity of using Eq. (51) for the evaluation of R_{ck} is concerned, it must be pointed out that Eq. (51) establishes a relationship between the cubic characteristic strength and the cylindrical strengths of core samples, while our experimentation was performed on casted specimens. It is well known that extracting a core sample damages the specimen to be tested, causing the compressive strength to decrease. According to DM 14/01/2008, the compressive strength measured on core samples must be increased by a factor F_{Tor}, called the torment factor, which is inversely proportional to the compressive strength itself (Tab. 7).

Now, since:

$$\frac{\min\{f_{c1}, f_{c2}\}}{1.02} > 40, \tag{63}$$

we fall into the last case presented in Tab. 7:

$$F_{Tor} = 1.00, \tag{64}$$

and Eq. (51) can be used for casted specimens without including any corrective factor.

Table 7: Torment factor in function of the compressive strength measured on core samples

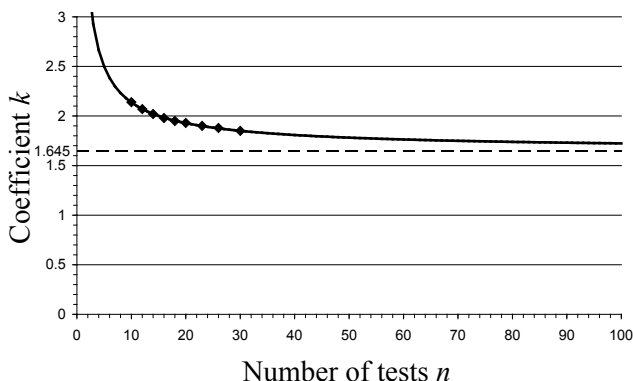| $f_{c,carrot} \ [N/mm^2]$	F_{Tor}
10-15	1.15
16-20	1.12
21-25	1.10
26-30	1.07
31-35	1.05
36-40	1.02
> 40	1.00

Figure 45: Interpolation of the coefficient k (90% confidence degree)
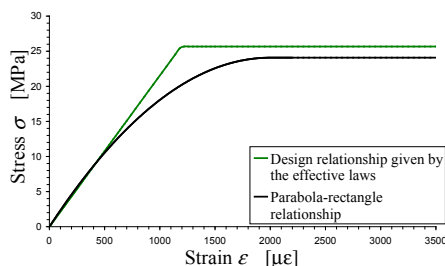
Figure 46: Comparison between the parabola-rectangle relationship and the design relationship given by the effective laws
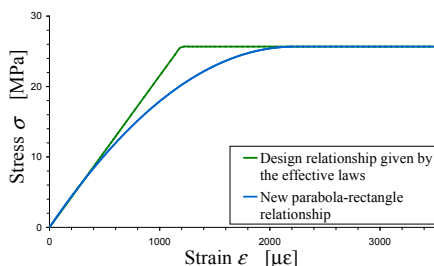
Figure 47: Comparison between the new parabola-rectangle relationship and the design relationship given by the effective laws

It must be noticed that the cylindrical design strength provided by Eq. (62) is not very far from the f_{cd} given by the statistical approach. Actually, by approximating the experimental data with a Gaussian distribution and interpolating the values of k in Tab. 4, we can estimate k for $n = 4$. The interpolation function of equation:

$$k = \frac{3.06748}{n^{0.794772}} + 1.645, \tag{65}$$

shown in Fig. 45 together with the interpolated data, gives the value:

$$k(n = 4) = 2.664. \tag{66}$$

This second time, the two cylindrical strengths, f_{c3} and f_{c4}:

$$f_{c3} = 46.65 \, N/mm^2, \tag{67}$$

$$f_{c4} = 48.70 \ N/mm^2, \tag{68}$$

can be converted into cubic strengths, R_{c3} and R_{c4}, and used together with the cubic strengths R_{c1} and R_{c2} of the two cubic specimens for evaluating R_{ck}. The $n = 4$ available cubic strengths are shown in Tab. 8.

Table 8: Cubic strengths for the evaluation of R_{ck}

$R_{c1} \ [N/mm^2]$	$R_{c2} \ [N/mm^2]$	$R_{c3} \ [N/mm^2]$	$R_{c4} \ [N/mm^2]$
54.06	58.08	56.21	58.68

The result is:

$$R_{cm} = 56.76 \ N/mm^2, \tag{69}$$

$$\delta = 2.09, \tag{70}$$

$$R_{ck} = 51.20 \ N/mm^2, \tag{71}$$

$$f_{cd} = 24.08 \ N/mm^2. \tag{72}$$

The parabola-rectangle relationship given by Eqs. (56) and (57), with f_{cd} provided by Eq. (72), is shown in Fig. 46.

For comparison purposes, in Fig. 46 a design relationship derived from the effective laws has also been plotted. This second design relationship is given by the two functions:

$$\sigma = \bar{\sigma}_{eff} \quad \varepsilon_c \leq 1.2\text{‰}, \tag{73}$$

$$\sigma = \sigma_{cd,eff} = \frac{0.85\sigma_{ck,eff}}{1.5} \quad 1.2\text{‰} < \varepsilon_c \leq 3.5\text{‰}, \tag{74}$$

where $\bar{\sigma}_{eff}$ is the average effective stress in Fig. 40 and $\sigma_{ck,eff}$ is the 5% lower fractile of the average effective stresses $\bar{\sigma}_{ci,eff}$, evaluated in the four pseudo-horizontal branches of the effective laws (Tab. 9).

Table 9: Average stresses in the pseudo-horizontal branches of the effective laws

$\bar{\sigma}_{c1,eff} \ [N/mm^2]$	$\bar{\sigma}_{c2,eff} \ [N/mm^2]$	$\bar{\sigma}_{c3,eff} \ [N/mm^2]$	$\bar{\sigma}_{c4,eff} \ [N/mm^2]$
55.30	57.05	49.39	54.55

The statistical approach for $k = 2.66$ gives:

$$\bar{\sigma}_{cm,eff} = 54.07 \ N/mm^2, \tag{75}$$

$$\delta = 3.29, \tag{76}$$

$$\sigma_{ck,eff} = \bar{\sigma}_{cm,eff} - k\delta = 45.30 \, N/mm^2, \tag{77}$$

$$\sigma_{cd,eff} = 25.67 \, N/mm^2. \tag{78}$$

As can be seen in Fig. 46, the parabola-rectangle relationship given by Eqs. (56) and (57) slightly overestimates the initial slope and underestimates the ultimate design stress. According to this analysis, we can conclude that the parabola-rectangle relationship is cautionary as far as the ultimate stress is concerned. It therefore seems that the identification procedure of the effective law may be employed for deriving a new parabola-rectangle relationship, to exploit the effective properties of concrete better.

As previously pointed out, the number of performed compression tests is not sufficient for giving quantitative evaluations. It follows that only a qualitative new proposal is possible here. The parabola-rectangle relationship that gives a better approximation to the design relationship given by the effective laws in Fig. 40 is plotted in Fig. 47 and is expressed by the function:

$$\sigma_c = 1000\sigma_{cd,eff}\left(0.9\varepsilon_c - 202.5\varepsilon_c^2\right) \quad \varepsilon_c \leq \frac{1}{450}, \tag{79}$$

for the first branch, and by the function:

$$\sigma_c = \sigma_{cd,eff} \quad \frac{1}{450} < \varepsilon_c \leq 3.5\text{‰}. \tag{80}$$

for the second branch. It is still a cautionary relationship, but the ultimate stress has been increased by 7%.
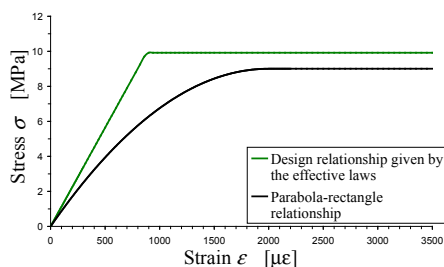

Figure 48: Comparison between the parabola-rectangle relationship and the design relationship given by the effective laws
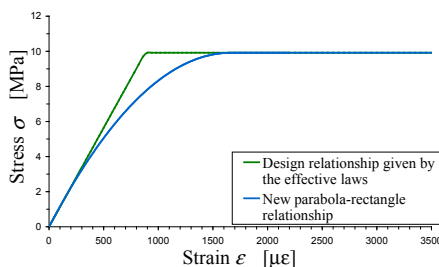
Figure 49: Comparison between the new parabola-rectangle relationship and the design relationship given by the effective laws

3.2 Rubberized concrete

For rubberized concrete, it is reasonable to assume that the design relationship depends upon the percentage of rubber aggregates. In the absence of a technical standard for rubberized concrete, the parabola-rectangle relationship in Fig. 48 has been drafted according to Eqs. (56) and (57), with the four R_{ci} obtained as for plain concrete and set out in Tab. 10.

Table 10: Cubic strengths for the evaluation of R_{ck}

$R_{c1}\ [N/mm^2]$	$R_{c2}\ [N/mm^2]$	$R_{c3}\ [N/mm^2]$	$R_{c4}\ [N/mm^2]$
20.10	21.81	21.05	21.40

The statistical approach with $k = 2.66$ provides:

$$R_{cm} = 21.09\ N/mm^2, \tag{81}$$

$$\delta = 0.73, \tag{82}$$

$$R_{ck} = 19.14\ N/mm^2, \tag{83}$$

$$f_{cd} = 9.00\ N/mm^2. \tag{84}$$

A possible standard for the percentage of rubber aggregates used is given by the relationship:

$$R_{ck} = \frac{1}{0.83} \min\{f_{cm} - 3;\ f_{c,lowest} + 2\}, \tag{85}$$

giving the following values for R_{ck} and f_{cd}:

$$R_{ck} = 17.47\ N/mm^2, \tag{86}$$

$$f_{cd} = 8.23\ N/mm^2. \tag{87}$$

In Fig. 48, the design relationship derived from the effective laws is given by the two functions:

$$\sigma = \bar{\sigma}_{eff} \quad \varepsilon_c \leq 0.88\text{\textperthousand}, \tag{88}$$

$$\sigma = \sigma_{cd,eff} = \frac{0.85\sigma_{ck,eff}}{1.5} \quad 0.88\text{\textperthousand} < \varepsilon_c \leq 3.5\text{\textperthousand}, \tag{89}$$

where $\bar{\sigma}_{eff}$ is the average effective stress in Fig. 43 and $\sigma_{ck,eff}$ is the 5% lower fractile of the average effective stresses $\bar{\sigma}_{ci,eff}$, evaluated in the four pseudo-horizontal branches of the effective laws (Tab. 11):

Table 11: Average stresses in the pseudo-horizontal branches of the effective laws

$\bar{\sigma}_{c1,eff}\ [N/mm^2]$	$\bar{\sigma}_{c2,eff}\ [N/mm^2]$	$\bar{\sigma}_{c3,eff}\ [N/mm^2]$	$\bar{\sigma}_{c4,eff}\ [N/mm^2]$
21.22	21.99	19.19	20.39

$$\bar{\sigma}_{cm,eff} = 20.70\ N/mm^2, \tag{90}$$

$$\delta = 1.20, \tag{91}$$

$$\sigma_{ck,eff} = \bar{\sigma}_{cm,eff} - k\delta = 17.50\ N/mm^2, \tag{92}$$

$$\sigma_{cd,eff} = 9.92\ N/mm^2. \tag{93}$$

As can be seen in Fig. 48, in this second occasion, the parabola-rectangle relationship underestimates both the initial slope and the ultimate stress.

The new parabola-rectangle relationship set out in Fig. 49 is given by the function:

$$\sigma_c = 1000\sigma_{cd,eff}\left(1.2\varepsilon_c - 360\varepsilon_c^2\right) \quad \varepsilon_c \leq \frac{1}{600}, \tag{94}$$

for the first branch, and by the function:

$$\sigma_c = \sigma_{cd,eff} \quad \frac{1}{600} < \varepsilon_c \leq 3.5\text{‰}, \tag{95}$$

for the design of the second branch. The new relationship (Fig. 49) fits the initial slope well and allows for an ultimate stress increment of 10%.

4   Conclusions

The experimentation presented here has shown that the effective law is also monotonically non-decreasing for rubberized concrete, besides offering the same relationship for both cubic and cylindrical specimens. This last result is of particular significance, since insensitiveness to shape-effect is one of the principle requirements for constitutive parameters, thereby describing the identification procedure of the effective law as a properly posed identification technique. As a consequence of these findings and of further properties of the effective law, as set out in previous papers by the author, we may conclude that the question of strain-softening, widely discussed in Ferretti (2005) from a numerical point of view, may have been resolved, with the identification procedure of the effective law producing final experimental evidence against its existence. Moreover, it has been also shown how the effective law is capable of providing an experimental evaluation of the design relationships, making it also possible to formulate new standards for both plain and rubberized concrete.

5 Future developments

The functions shown in Eqs. (94) and (95) give a good design relationship for the rubber percentage used in this experimentation only. Further experiments with differing amounts of rubber aggregates are needed to derive a design relationship that is also a function of the rubber percentage.

References

Bažant, Z. P. (1991): Why Continuum Damage is Nonlocal: Micromechanics Arguments. *J. Eng. Mech.*, 117(5): 1070-1087.

Bažant, Z. P. (1994): Nonlocal Damage Theory based on Micromechanics of Crack Interactions. *J. Eng. Mech.*, 120(3): 593-617.

Bažant, Z. P.;, Belytschko, T. B.; Chang, T. P. (1984): Continuum Model for Strain Softening. *J. Eng. Mech.*, 110(12): 1666-1692.

Bažant, Z. P.; and Chang, T. P. (1984): Is Strain-Softening Mathematically Admissible? *Proc., 5th Engineering Mechanics Division*, 2, 1377-1380.

Bažant, Z. P.; Jirásek, M. (2002): Nonlocal Integral Formulations of Plasticity and Damage: Survey of Progress. *J. Eng. Mech.*, 128(11): 1119-1149.

Bažant, Z. P.; Lin, F.–B. (1988a): Nonlocal Smeared Cracking Model for Concrete Fracture. *J. Struct. Eng.*, 114(11): 2493-2510.

Bažant, Z. P.; Lin, F.–B. (1988b): Nonlocal Yield-Limit Degradation. *Int J. Numer. Methods Eng.*, 26: 1805-1823.

Bažant, Z. P.; Ožbolt, J. (1990): Nonlocal Microplane Model for Fracture, Damage, and Size Effect in Structures. *J. Eng. Mech.*, 116(11): 2485-2505.

Bažant, Z. P.; Pijaudier-Cabot, G. (1988): Nonlocal Continuum Damage, Localization Instability and Convergence. *J. Appl. Mech*, 55:, 287-293.

Bažant, Z. P.; Pijaudier-Cabot, G. (1989): Measurement of the Characteristic Length of Nonlocal Continuum. *J. Eng. Mech.*, 113: 2333-2347.

Bažant, Z. P.; Tabbara, M. R.; Kazemi, M. T.; Pijaudier-Cabot, G. (1990): Random Particle Model for Fracture of Aggregate or Fiber Composites. *J. Eng. Mech.*, 116(8): 1686-1705.

Bergan, P.G. (1983): Record of the Discussion on Numerical Modeling. *IUTAM W. Prager Symposium*, Northwestern University, Evanston, Ill.

Borino, G.; Fuschi, P.; Polizzotto, C. (1999): A Thermodynamic Approach to Nonlocal Plasticity and Related Variational Approaches. *J. Appl. Mech.*, 66: 952-963.

Brace, W. F., Paulding, B. W. and Scholz, C. (1966): Dilatancy in the Fracture of

Crystalline Rocks. *J. Geophys. Res.*, vol. 71, no. 16, pp. 3939-3953.

Chandrasekhar, S. (1950): *Radiation Transfer*, Oxford University Press, London.

Chen, J.–S.; Wu, C.–T.; Belytschko, T. (2000): Regularization of Material Instabilities by Meshfree Approximations with Intrinsic Length Scales. *Int. J. Numer. Meth. Engng.*, 47: 1303-1322.

Daponte, P. and Olivito, R.S. (1989): Crack Detection Measurements in Concrete. *ISMM International Conference Microcomputers Applications*, pp. 123-127.

Di Leo, A., Di Tommaso, A. and Merlari, R. (1979): Danneggiamento per Microfessurazione di Malte di Cemento e Calcestruzzi Sottoposti a Carichi Ripetuti. *Technical Note 46* (in Italian), DISTART – University of Bologna, Italy.

Dresher, A. and Vardoulakis, I. (1982): Geometric Softening in Triaxial Tests on Granular Material. *Geotechnique*, 32(4): 291-303.

Drugan, W. J.; Willis, J. R. (1996). A Micromechanics-Based Nonlocal Constitutive Equation and Estimates of Representative Volume Element Size for Elastic Composites. *J. Mech. Phys. Solids*, 44: 497-524.

Duhem, P. (1893): Le Potentiel Thermodynamique et la Pression Hydrostatique. *Ann. Sci. Ecole Norm. S.*, 10: 183-230.

Edelen, D. G. B.; Green, A. E.; Laws, N. (1971): Nonlocal Continuum Mechanics. *Arch. Ration. Mech. Anal.*, 43: 36-44.

Eringen, A. C. (1966): A Unified Theory of Thermomechanical Materials. *Int. J Eng. Sci.*, 4:, 179-202.

Eringen, A. C. (1972): Linear Theory of Nonlocal Elasticity and Dispersion of Plane Waves. *Int. J Eng. Sci.*, 10:, 425-435.

Eringen, A. C. (1981): On Nonlocal Plasticity. *Int. J Eng. Sci.*, 19: 1461-1474.

Eringen, A. C. (1983): Theories of Nonlocal Plasticity. *Int. J Eng. Sci.*, 21: 741-751.

Eringen, A. C.; Edelen, D. G. B. (1972): On Nonlocal Elasticity. *Int. J Eng. Sci.*, 10: 233-248.

Eringen, A. C.; Kim, B. S. (1974): Stress Concentration at the Tip of a Crack. *Mech. Res. Commun.*, 1: 233-237.

Eringen, A. C.; Speziale, C. G.; Kim, B. S. (1977): Crack-Tip Problem in Nonlocal Elasticity. *J. Mech. Phys. Solids*, 25: 339-355.

Ferretti, E. (2001): *Modellazione del Comportamento del Cilindro Fasciato in Compressione*. Ph.D. Thesis (in Italian), University of Lecce, Italy.

Ferretti, E. (2003): Crack Propagation Modeling by Remeshing using the Cell Method (CM). *CMES: Computer Modeling in Engineering & Sciences*, vol. 4, no.

1, pp. 51-72.

Ferretti, E. (2004a): A Discussion of Strain-Softening in Concrete. *Int. J. Fracture* (Letters section), vol. 126, no. 1, pp. L3-L10.

Ferretti, E. (2004b): Experimental Procedure for Verifying Strain-Softening in Concrete. *Int. J. Fracture* (Letters section), vol. 126, no. 2, pp. L27-L34.

Ferretti, E. (2004c): On Poisson's Ratio and Volumetric Strain in Concrete. *Int. J. Fracture* (Letters section), vol. 126, no. 3, pp. L49-L55.

Ferretti, E. (2004d): Crack-Path Analysis for Brittle and Non-Brittle Cracks: a Cell Method Approach. *CMES: Computer Modeling in Engineering & Science*, vol. 6, no. 3, pp. 227-244.

Ferretti, E. (2004e): A Cell Method (CM) Code for Modeling the Pullout Test Step-Wise. *CMES: Computer Modeling in Engineering & Science*, vol. 6, no. 5, pp. 453-476.

Ferretti, E. (2005): A Local Strictly Nondecreasing Material Law for Modeling Softening and Size-Effect: a Discrete Approach. *CMES: Computer Modeling in Engineering & Science*, vol. 9, no. 1, pp. 19-48.

Ferretti, E. (2009): Cell Method Analysis of Crack Propagation in Tensioned Concrete Plates. *CMES: Computer Modeling in Engineering & Science*, vol. 54, no. 3, pp. 253-282.

Ferretti, E. (2012a): Waste Tire Rubberized Concrete Plates for Airport Pavements: Stress and Strain Profiles in Time and Space Domains. *CMC: Computers, Materials, & Continua*, in press.

Ferretti, E. (2012b): A Higher Order Solution of the Elastic Problem for a Homogeneous, Liear-Elastic, and Isotropic Half-Space Subjected to a Point Load. *CMES: Computer Modeling in Engineering & Science*, in press.

Ferretti, E. and Bignozzi, M.C. (2011): In-Situ Mechanical Characterization of Waste Tire Rubberized Concrete (PFU) for Airport Pavements. *Proc. AIMETA 2011*, Bologna, Italy, September 12-15, pp. 1-10.

Ferretti, E. and Bignozzi, M.C. (2012): Stress and Strain Profiles along the Cross-Section of Waste Tire Rubberized Concrete Plates for Airport Pavements. *CMC: Computers, Materials, & Continua*, vol. 27, no. 3, pp. 231-274.

Ferretti, E., Casadio, E. and Di Leo, A. (2008): Masonry Walls under Shear Test: a CM Modeling. *CMES: Computer Modeling in Engineering & Science*, vol. 30, no. 3, pp. 163-190,.

Ferretti, E. and Di Leo, A. (2003): Modelling of Compressive Tests on FRP Wrapped Concrete Cylinders through a Novel Triaxial Concrete Constitutive Law. *SITA*, vol. 5, pp. 20-43.

Ferretti, E. and Di Leo, A. (2008): Cracking and Creep Role in Displacements at Constant Load: Concrete Solids in Compression. *CMC: Computers, Materials, & Continua*, vol. 7, no. 2, pp. 59-80.

Gao, H.; Huang, Y. (2001): Taylor-Based Nonlocal Theory of Plasticity. *Int. J. Solids Struct.*, 38: 2615-2637.

Hadamard, J. (1903): *Leçons sur la Propagation des Ondes – Chapter VI*, Paris, France.

Hegemier, G. A. and Read, H. E. (1983): Some Comments on Strain-Softening. *DARPA-NSF Workshop*, Northwestern University, Evanston, Ill.

Hodgkin, A. L. (1964): *The Conduction of Nervous Impulses*, Thomas, Springfield, Ill.

Hu, X. Z.; Wittmann, F. H. (2000): Size Effect on Toughness Induced by Cracks Close to Free Surface. *Eng. Fract. Mech.*, 65: 209-211.

Hudson, J. A., Brown, E. T. and Fairhurst, C. (1971): Shape of the Complete Stress-Strain Curve for Rock. 13th *Symposium on Rock Mechanics*, University of Illinois, Urbana, Ill.

Huerta, A.; Pijaudier-Cabot, G. (1994): Discretization Influence on Regularization by two Localization Limiters. *J. Eng. Mech.*, 120(6): 1198-1218.

Jirásek, M. (1998a): Embedded Crack Models for Concrete Fracture. In: *Computational Modelling of Concrete Structures*, R. de Borst, N. Bi?ani?, H. Mang, and G. Meschke eds., Balkema, Rotterdam, 291-300.

Jirásek, M. (1998b): Nonlocal Models for Damage and Fracture: Comparison of Approaches. *Int. J. Solids Struct.*, 35: 4133-4145.

Jirásek, M. (1999): Computational Aspects of Nonlocal Models. *Proc.*, *ECCM '99*, München, Germany, 1-10.

Jirásek, M.; Bažant, Z. P. (1995): Macroscopic Fracture Characteristics of Random Particle Systems. *Int. J. Fract.*, 69: 201-228.

Jirásek, M.; Bažant, Z. P. (2001): *Inelastic Analysis of Structures*, John Wiley and Sons.

Jirásek, M.; Patzák, B. (2002): Consistent Tangent Stiffness for Nonlocal Damage Models. *Comput. Struct.*, in press.

Jirásek, M.; Rolshoven, S. (2002): Comparison of Integral-Type Nonlocal Plasticity Models for Strain-Softening Materials. *Preprint submitted to Elsevier Science*, 1-63.

Jirásek, M.; Zimmermann, T. (1998): Rotating Crack Model with Transition to Scalar Damage. *J. Eng. Mech.*, 124(3), 277-284.

Kröner, E. (1968): Elasticity Theory of Materials with Long-Range Cohesive Forces. *Int. J. Solids Struct.*, 3: 731-742.

Krumhansl, J. A. (1965): Generalized Continuum Field Representation for Lattice Vibrations. In *Lattice dynamic*s, R. F. Wallis ed., Pergamon, London, pp. 627-634.

Kunin, I. A. (1966): Theory of Elasticity with Spatial Dispersion. *Prikl. Mat. Mekh.* (in Russian), 30: 866.

La Tegola, A. (1977): *Teoria semiprobabilistica della sicurezza nel calcolo agli stati limite delle strutture in cemento armato*, Bari (Italy), Adriatica Ed.

Leblond, J. B.; Perrin, G.; Devaux, J. (1994): Bifurcation Effects in Ductile Metals Incorporating Void Nucle-Ation, Growth and Interaction. *J. Appl. Mech.*, Bifurcation effects in ductile metals with nonlocal damage, 236-242.

Luciano, R.; Willis, J. R. (2001): Nonlocal Constitutive Response of a Random Laminate Subjected to Configuration-Dependent Body Force. *J. Mech. Phys. Solids*, 49: 431-444.

Needleman, A.; Tvergaard, V. (1998): Dynamic Crack Growth in a Nonlocal Progressively Cavitating Solid. *Eur. J. Mech. A–Solid*, 17: 421-438.

Nilsson, C. (1994): On Local Plasticity, Strain Softening, and Localization. *Rep., No. TVSM-1007*, Division of Structural Mechanics, Lund Institute of Technology, Lund, Sweden.

Nilsson, C. (1997): Nonlocal Strain Softening Bar Revisited. *Int. J. Solids Struct.*, 34: 4399-4419.

Noll, W. (1972): A new Mathematical Theory of Simple Materials. *Arch. Ration. Mech. Anal.*, vol. 48, pp. 1-50.

Oseen, C. W. (1933): The Theory of Liquid Crystals. *Trans. Faraday Soc.*, 29: 883-899.

Ožbolt, J.; Bažant, Z. P. (1996): Numerical Smeared Fracture Analysis: Nonlocal Microcrack Interaction Approach. *Int. J. Numer. Methods Eng.*, 39: 635-661.

Pijaudier-Cabot, G.; Bažant, Z. P. (1987): Nonlocal Damage Theory. *J. Eng. Mech.*, 113: 1512-1533.

Planas, J.; Elices, M.; Guinea, G. V. (1993): Cohesive Cracks versus Nonlocal Models: Closing the Gap. *Int J. Fract.*, 63: 173-187.

Planas, J.; Guinea, G. V.; Elices, M. (1996): Basic Issues on Nonlocal Models: Uniaxial Modeling. *Tech. Rep., No. 96-jp03*, Departamento de Ciencia de Materiales, ETS de Ingenieros de Caminos, Univ. Politécnica de Madrid, Ciudad Univ. sn., 28040 Madrid, Spain.

Rayleigh, O. M. (1918): Notes on the Theory of Lubrication. *Philos. Mag.*, 35:

1-12.

Rogula, D. (1965): Influence of Spatial Acoustic Dispersion on Dynamical Properties of Dislocations. I. *Bulletin de l'Académie Polonaise des Sciences*, *Séries des Sciences Techniques*, 13: 337-343.

Rogula, D. (1982): Introduction to Nonlocal Theory of Material Media. In *Nonlocal theory of material media*, *CISM courses and lectures*, D. Rogula ed., Springer, Wien, 268: 125-222.

Sandler, I. and Wright, J. P. (1983): Summary of Strain-Softening. *DARPA-NSF Workshop*, Northwestern University, Evanston, Ill.

Saouridis, C. (1988): *Identification et Numérisation Objectives des Comportements Adoucissants: une Approche Multiéchelle de l'Endommagement du Béton*, Ph.D. Thesis, Univ. Paris VI, France.

Saouridis, C.; Mazars, J. (1992): Prediction of the Failure and Size Effect in Concrete via a Biscale Damage Approach. *Eng. Comput.*, 9: 329-344.

Schlangen, E., (1993): *Experimental and Numerical Analysis of Fracture Processes in Concrete*, Ph.D. Thesis, Delft Univ. of Technology, Delft, The Netherlands.

Schlangen, E.; van Mier, J. G. M. (1992): Simple Lattice Model for Numerical Simulation of Fracture of Concrete Materials and Structures. *Mater. Struct.*, 25: 534-542.

Strömberg, L.; Ristinmaa, M. (1996): FE Formulation of a Nonlocal Plasticity Theory. *Comput. Methods Appl. Mech. Eng.*, 136: 127-144.

Tvergaard, V.; Needleman, A. (1995): Effects of Nonlocal Damage in Porous Plastic Solids. *Int. J. Solids Struct.*, 32: 1063-1077.

van Mier, J. G. M. (1997): *Fracture Processes of Concrete*, CRC, Boca Raton, Fla.

Vermeer, P. A.; Brinkgreve, R. B. J. (1994): A new Effective Non-Local Strain Measure for Softening Plasticity. In *Localization and Bifurcation Theory for Solis and Rocks*, R. Chambon, J. Desrues, and I. Vardoulakis eds., Balkema, Rotterdam, The Netherlands, 89-100.

Wu, F. H. and Freud, L.B. (1983): *Report MRL-E-145*, Brown University, Providence, RI, USA.